

Artificial Phototropism Based on a Photo–Thermo–Responsive Hydrogel

by

Hamsini Gopalakrishna

A Thesis Presented in Partial Fulfillment
of the Requirements for the Degree
Master of Science

Approved April 2016 by the
Graduate Supervisory Committee:

Ximin He, Chair
Liping Wang
Zachary Holman

ARIZONA STATE UNIVERSITY

May 2016

ABSTRACT

Solar energy is leading in renewable energy sources and the aspects surrounding the efforts to harvest light are gaining importance. One such aspect is increasing the light absorption, where heliotropism comes into play. Heliotropism, the ability to track the sun across the sky, can be integrated with solar cells for more efficient photon collection and other optoelectronic systems. Inspired by plants, which optimize incident sunlight in nature, several researchers have made artificial heliotropic and phototropic systems. This project aims to design, synthesize and characterize a material system and evaluate its application in a phototropic system. A gold nanoparticle (Au NP) incorporated poly(N-isopropylacrylamide) (PNIPAAm) hydrogel was synthesized as a photo-thermo-responsive material in our phototropic system. The Au NPs generate heat from the incident via plasmonic resonance to induce a volume phase change of the thermo-responsive hydrogel PNIPAAm. PNIPAAm shrinks or swells at temperature above or below 32°C. Upon irradiation, the Au NP-PNIPAAm micropillar actuates, specifically bending toward the incident light and precisely following the varying incident angle.

Swelling ratio tests, bending angle tests with a static incident light and bending tests with varying angles were carried out on hydrogel samples with varying Au NP concentrations. Swelling ratios ranging from 1.45 to 2.9 were recorded for pure hydrogel samples and samples with very low Au NP concentrations. Swelling ratios of 2.41 and 3.37 were calculated for samples with low and high concentrations of Au NPs, respectively. A bending of up to 88° was observed in Au NP-hydrogel pillars with a low Au NP concentration with a 90° incident angle. The light tracking performance was assessed by

the slope of the pillar Bending angle (response angle) vs. Incident light angle plot. A slope of 1 indicates ideal tracking with top of the pillar being normal to the incident light, maximizing the photon absorption. Slopes of 0.82 and 0.56 were observed for the low and high Au NP concentration samples. The rapid and precise incident light tracking of our system has shown the promise in phototropic applications.

DEDICATION

To my mother and father,
for all that you have taught me,
your unconditional love, kindness, patience and support.

ACKNOWLEDGMENTS

I thank my graduate advisor Dr. Ximin He for her meaningful suggestions, interest and time. She has motivated, inspired and guided me all the way. I acknowledge the support and timely help obtained from the committee members Dr. Zachary Holman and Dr. Liping Wang. I appreciate greatly being able to use the equipment in Dr. Holman's lab. I also thank Christine Quintero and the SEMTE graduate office staff for their patient help with the paperwork and ensuring that I was on track with coursework and other requirements.

I want to thank the post doctoral researcher Dr. Zhi Zhao, for his guidance, Hanqing Nan, Tianxiang Gao, Maritza Mujieca and Maya Castro for all their help and support. I particularly thank Weston Michl for his help with my project.

I thank the many friends from ASU with whom I discussed various issues, at all times of day and night, and in particular my fiancé Joe Victor Carpenter III for his constant support and love.

Last but certainly not least, I thank my parents and family for having faith in me and supporting me.

TABLE OF CONTENTS

	Page
LIST OF TABLES	vii
LIST OF FIGURES	viii
1 INTRODUCTION	1
1.1 Motivation.....	1
1.2 Background.....	5
1.2.1 Polymers and Hydrogels	5
1.2.2 Smart Hydrogels	5
1.2.3 Light Scattering by Particles and Localized Surface Plasmon Resonance	8
1.2.4 General Characterization and Fabrication Methods	11
1.3 Novelty: Combining the Ingredients.....	13
2 METHODOLOGY AND EXPERIMENTATION	14
2.1 Materials	14
2.1.1 Chemicals.....	14
2.1.2 Instruments.....	14
2.1.3 Recipes.....	15
2.1.4 Softwares.....	17
2.2 Experimental Procedure.....	17

	Page
2.2.1 Background Study.....	18
2.2.2 Focused Study.....	24
3 RESULTS AND DISCUSSION.....	29
3.1 Background Study.....	29
3.1.1 Characterization Of Au NPs With Varying Stirring Times.....	29
3.1.2 Characterization of Au NPs With Varying Reducing Agents.....	31
3.1.3 Swelling ratio tests: Low Au NP Concentration Samples.....	33
3.2 Focused Study.....	39
3.2.1 Swelling Ratio Tests: High Au NP Concentration Samples – Heat Actuated.	40
3.2.2 Swelling Ratio Tests: High Au NP Concentration Samples – Light Actuated	41
3.2.3 Bending Angle Tests.....	42
3.2.4 Variable Angle Tests.....	45
4 CONCLUSIONS AND FUTURE WORK.....	47
REFERENCES.....	50

LIST OF TABLES

Table	Page
1: Conversion Between a Volume Based and Absolute Au Concentration in the System	20
2: Composition of the Macro-Samples Used for Testing with Halogen and LED Lamps	22
3: Comparative Study of Light Intensities and Au NP Concentrations	23
4: Calculated Intensities for the Laser Powers used in Experiments	26
5: Au NP Batches with Varying Stirring Times Along with Their Particle Sizes	28
6: Summary of Au NP Sizes for Batches with Lower Trisodium Citrate	30
7: Averaged Swelling Ratios from Constrained and Unconstrained Samples	33
8: Summary of the macro-sample test results illuminated with the halogen lamp.....	35
9: Summary of Unconstrained Swelling Ratio Results	40
10: Summary of the Trendlines for the 10x Sample	42
11: Change in the Bending Angle for the 20x Sample	42
12: Incident and Response Angles for the 10x and 20x Samples	44

LIST OF FIGURES

Figure	Page
1: Schematic of the Bending Mechanism in Plants by a Gradient of Auxins.....	1
2: Reproduced Figure of the Heliotropic System Presented by Li et al. The Solar Panel is Held by Six Actuator Beams that Actuate (Shrink) when the Incident Sunlight Increases the Temperature to Above 68°C.	2
3: Schematic of the Sunsaluter Which Utilizes Weights That Shift During the Day to Adjust the Tilt of the Solar Panels. Potable Water is a Byproduct of this Process.....	3
4: Schematic of the Bending Mechanism in the Proposed System. The Heat Generated from the Gold Nanoparticle Actuates the Hydrogel.	4
5: Schematic Illustrating the Lower Critical Solution Temperature (a) And the Upper Critical Solution Temperature of Polymers (b). The Structure of Poly(N-Isopropylacrylamide) is also Shown (c).	6
6: Schematic Showing the Collapsed (Above 32°C) and Swollen States (Below 32°C) of the Poly(N-Isopropylacrylamide) Hydrogel.	7
7: Illustration of Surface Plasmons (a) and a Localized Surface Plasmon (b).....	9
8: Photograph Showing the Color of Colloidal Gold Based on Particle Size.....	11
9: Schematic of the Working of the Projection Micro Stereo Lithography. The Image of the Sample to be Printed is Projected on the Stage.....	12
10: Photograph of the Setup for Constrained Cooling Curve Swelling Ratio Tests.....	20
11: Photograph of the Setup for the Unconstrained Swelling Ratio Tests	20

Figure	Page
12: Schematic Showing the Polydimethylsiloxane:Glass Slide Method in Which the Silanized Glass Slide Placed in the Slot in (a) Adheres to the Hydrogel Solution Introduced in (b). Photograph of the Final Sample (c) and the Test Setup for Macro-Samples (D)	22
13: Design of the Pillar Sample Used for Bending Angle and Variable Angle Tests	24
14: Setup for Tte Laser Induced Swelling Ratio Tests. The Red Glasses are Laser Protective and Prevent the Microscope Charged Coupled Device from Saturating.	26
15: Photographs of the Sample in the Glass Case. (a) The Laser Comes in from the Right. Overlay in (b) Shows the Measurement of the Bending Angle (Θ_b). The Image Appears Red Since Laser Protective Red Glasses were Placed in Front of the Camera.....	27
16: Schematic for the Variable Angle Testing (a). Photograph of the Samples Illuminated With Laser Overlaid With the Measurements of the Incident Angle Θ_i (B) and the Response Angle Θ_r (C).....	28
17: UV-Vis Spectrophotometer Absorption Curves for the First Four Batches of Particles Prepared. They were Stirred for 10 Minutes (a), 20 Minutes (b), 25 Minutes (c) And 30 Minutes (d). The Particle Size is Unaffected by Different Stirring Times.	30
18: UV-Vis Spectrophotometer Absorption Graphs Of The Last Two Batches With One Fifth the Sodium Citrate Amount (a) And Half the Sodium Citrate Amount (b).	31
19: SEM Images of Gold Nanoparticles Fabricated in the Lab. Image on the Right Shows NaCl Crystals in the Sample Despite Being Twice Rinsed in DI Water.	32
20: DLS Results Showing the Particle Diameter of the Gold Nanoparticles.	33

Figure	Page
21: Normalized Swelling Ratio Test Results for Varying Au NP Concentrations	34
22: Schematic of a Bilayer with Different Stiffnesses Bending in Response to Stimuli ..	39
23: Optical Microscope Images of the 10x (a), (b) and 20x (c), (d) Samples Used for the Unconstrained Swelling Ratio Tests. Scale Bar is 500 μm . Normalized Swelling Ratio Tests of the 10x and 20x Samples. Data From the Pure Hydrogel Unconstrained Swelling Ratio Tests is also Included for Reference.	40
24: Photographs of the Laser Actuated Bending Angle Samples. Notice the Difference in the Intensities Before and After it Passes Through the Sample.....	42
25: Bending Angle vs. Time Graph for the 10x Sample (a) and the 20x Sample (b). Note the Time Scale Difference in (a) and (b).	43
26: Plots Showing the Correlation Between the Incident Angle and the Response Angle from the Samples	45

Chapter 1: INTRODUCTION

1.1 Motivation

Phototropism is the ability to track light whereas heliotropism is the ability of a plant or a structure to track the sun. Two types of heliotropism are seen in nature; floral and leaf heliotropism. In floral heliotropism, sunflowers, snow buttercups, arctic poppies and other flowers track the sun to increase the temperature of their centers. The heat attracts insects to the centers enhancing the chances of pollination.¹ Floral heliotropism can result in photosynthesis by active green ovary tissue. In leaf heliotropism, the leaf orientation changes throughout the day to increase incident light and photosynthesis. Leaf heliotropism is especially useful under shady conditions or during short growing periods. Both floral and leaf heliotropism is termed natural heliotropism.¹ Plants are thought to exhibit phototropism by a gradient of auxins (plant hormones) within the stem which promote asymmetrical growth response as illustrated in Figure 1.²

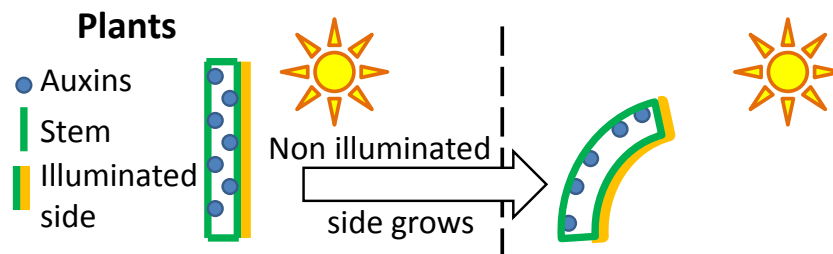


Figure 1: Schematic of the bending mechanism in plants by a gradient of auxins

Artificial heliotropic systems mimic nature's heliotropic response and can be active (external power driven) or passive (gravity, weights, heat or light driven). In comparison to a fixed solar panel, a dual-axis tracking solar panel receives about 34% more light.³

Heliotropism increases the efficiency of a solar module by maximizing the available light for electron-hole pair generation. Most active heliotropic systems that are used with solar panels have external positioning panels with motors,⁴ GPS tracking devices⁵ and need regular maintenance. Integrating the heliotropic property into the system material renders the system passive, reducing extraneous parts.

There are some heliotropic and phototropic systems demonstrated by other researchers which are described below. Li et al.,⁶ demonstrated a composite material heliotropic system while some students from MIT developed a bimetallic system. An individual from Princeton designed a system that is driven by weights and also purifies water during the day. Keeping the existing available systems in mind, a different material system with the potential to exhibit heliotropic behavior is explored in this project.

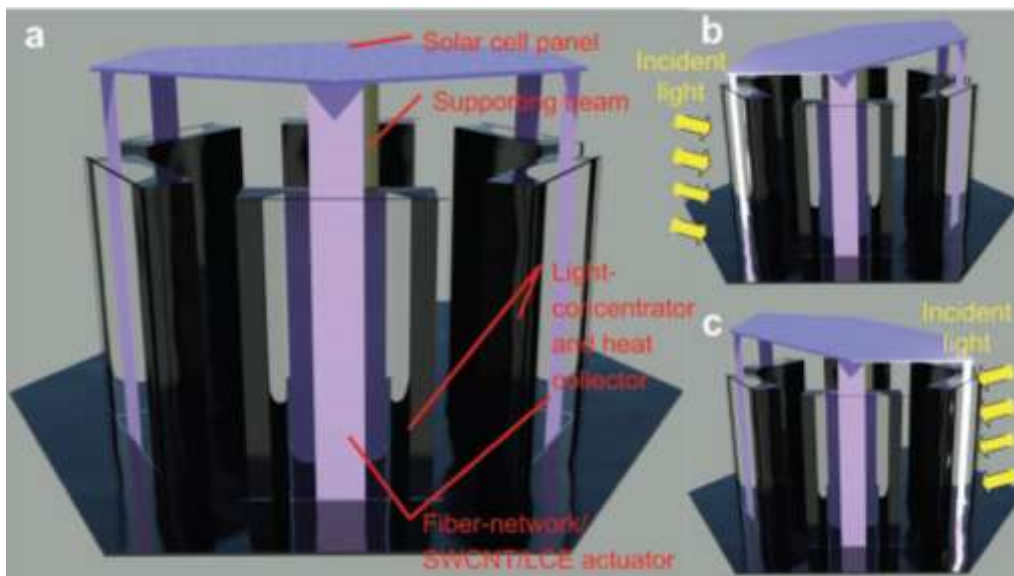


Figure 2: Reproduced figure of the heliotropic system presented by Li et al.⁶ The solar panel is held by six actuator beams that actuate (shrink) when the incident sunlight increases the temperature to above 68°C.

Li et al,⁶ demonstrated an artificial heliotropic system with a liquid crystalline elastomer for mechanical actuation, single wall carbon nanotubes for photo-thermal energy conversion and a polyurethane mesh for structural support. The elastomer, when heated above 68°C, changes its nematic order leading to a reversible axial contraction and mechanical actuation enabling the system to be heliotropic. Six panels made from this material support a solar module and move to track the sun as shown in Figure 2. In 2008, a student group from MIT⁷ developed a heliotropic system with aluminum and steel. The mechanism relies on difference in the coefficients of thermal expansion of the two metals. The expansion is caused by the temperature gradient between sunny and shaded areas. Eden Goh, a student from Princeton University⁸ developed a heliotropic system that uses water as weights to rotate the solar panel in 2008. In addition to increasing electricity generation, it also provides potable water as a byproduct.



Figure 3: Schematic of the SunSaluter which utilizes weights that shift during the day to adjust the tilt of the solar panels. Potable water is a byproduct of this process.⁹

A novel phototropic system with two components is proposed in this project. Noble metal nanoparticles—which absorb light via plasmonic resonance modes and generate heat—and a polymer that changes its volume in response to a temperature change are coupled to

produce a phototropic system with a tunable response time. The extent of bending of the sample can be controlled by the incident light angle. The system mimics heliotropism exhibited by plants by inducing a temperature gradient across the sample. The centimeter scale samples require no assembly after a simple two step fabrication process. Compared to other existing systems, our system has a much lower actuation temperature of 32°C, has fewer components in the system and is easier to fabricate. The reaction time is less than 10 seconds and is tunable. Though the hydrogel will be submerged in water, its phototropic response is not affected.

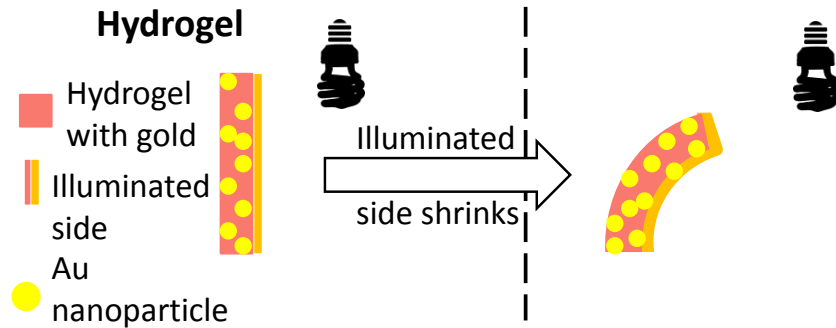


Figure 4: Schematic of the bending mechanism in the proposed system. The heat generated from the gold nanoparticle actuates the hydrogel.

The material utilizes the thermo-responsiveness of the well-studied, smart hydrogel poly(N-isopropylacrylamide) (PNIPAAm) with the photo-responsiveness of gold nanoparticles (Au NPs) to create a system with tunable response time. The work in this thesis takes a primary step towards using the hydrogel-nanoparticle system for phototropic applications and shows the tunability of the response time by varying the concentration of the Au NPs and the intensity of the incident light.

1.2 Background

1.2.1 Polymers and hydrogels

Polymers are long chains of chemically linked repeat units called monomers. Polymers are classified into linear, branched and crosslinked polymers based on their structure.¹⁰ Polymerization happens through three steps: initiation, propagation and termination.¹¹ The process of fibers entangling and trapping the solvent through surface tension is called gelation.¹² Hydrogels which are a binary polymer-solution 3D network, are capable of absorbing and retaining water.^{13,14} They can retain up to 20 times their dry-weight in water and are often biocompatible.¹⁵ Hydrogels can be physically (reversibly) crosslinked or chemically (irreversibly) crosslinked. The elasticity of the polymer gel depends on the volume of solvent and flexibility of the polymer chains.¹⁶

1.2.2 Smart hydrogels

Hydrogels can be conventional or stimulus responsive (smart) hydrogels. Smart hydrogels rapidly change their equilibrium state in response to external stimuli such as pH, temperature, electric field, magnetic field, bio-molecules, solvent, light, pressure, ionic strength of the solvent and presence of certain enzymes.^{15,17} The response to stimulus in smart hydrogels enables applications in responsive bio-interfaces, controlled drug-delivery,^{18,19} interactive coatings, microelectromechanical systems,^{20,21} diagnostics,²² smart optical systems,²³ thin film sensors,²² synthetic skin,²⁴ contact lenses,¹⁹ wound healing,²⁵ for cell adhesion,²² actuators²⁶ and other fields.

HEAT RESPONSIVE HYDROGELS

Smart hydrogels responsive to heat are called thermo-responsive hydrogels and the solubility of polymer changes with temperature. The lower and upper boundaries of solubility are called lower critical solution temperature (LCST) and upper critical solution temperature (UCST), respectively (see Figure 5). LCST and UCST refer to the temperatures below and above which the polymer and solvent are miscible. Above the LCST and below the UCST, the hydrogel network becomes immiscible.²⁷ The swelling/shrinking ratio of a hydrogel is the ratio of the dimensions of the hydrogel above and below its LCST/UCST and is usually measured volumetrically,^{28,29} linearly²³ or by weight.^{30,31}

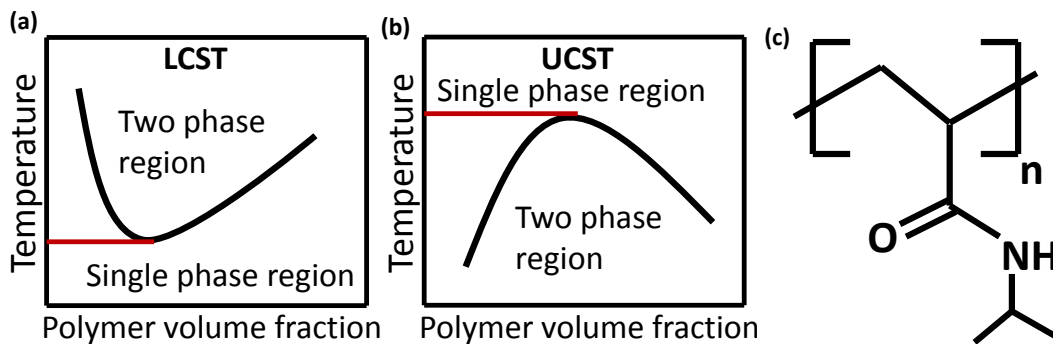


Figure 5: Schematic illustrating the LCST (a) and the UCST of polymers²⁷ (b). The structure of PNIPAAm is also shown (c).

PNIPAAm HYDROGEL

PNIPAAm (Figure 5c), is a commonly studied hydrogel due to its thermo-responsiveness.^{32,20} PNIPAAm has mechanical properties similar to human tissue, making it important in biomedical engineering. The LCST of PNIPAAm is around 32°C^{33,34} which is close to both room (22°C – 25°C) and human body temperatures (37°C).³⁵ Below the LCST, the hydrogel is hydrophilic and soluble. Above the LCST, the

hydrogel becomes hydrophobic and collapses becoming insoluble.³⁶ The change in volume is called the coil to globule transition³⁷ and is reversible.³⁸ The water in the hydrogel is expelled during the transition (mechanism shown in Figure 6). The combination of mechanical properties and thermo-responsive behavior makes PNIPAAm very lucrative for bio-applications such as artificial muscle,^{17,39,40,41} switches,⁴² controlled drug delivery systems,²³ scaffolding for tissue and cell growth.^{43,44,18} Henceforth in this document, PNIPAAm refers to the hydrogel of PNIPAAm and not just the polymer of NIPAAm.

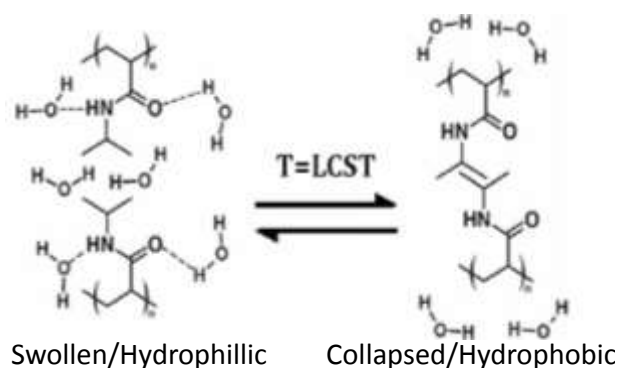


Figure 6: Schematic showing the collapsed (above 32°C) and swollen states (below 32°C) of the PNIPAAm hydrogel.

The transition below and above the LCST can be explained by a change in the osmotic pressure. The phase transition has been analyzed in terms of the osmotic pressure is given by the Flory-Rehner equation.⁴⁵ The swelling equilibrium criterion was developed into a theory by Flory and Rehner and is based on two properties of elastomers; their ability to absorb large amount of solvent without dissolving and their ability to undergo large deformations with small stresses.⁴⁶

$$\Pi = \frac{n_p k_b T}{V_0} \left[\frac{\phi}{2\phi_0} - \sqrt[3]{\frac{\phi}{\phi_0}} \right] - \frac{k_b T}{v_c} [\chi\phi^2 + \ln(1-\phi) + \phi]$$

Equation 1: Osmotic pressure and its relation to volume fraction

Here, Π is the osmotic pressure, ϕ is the volume fraction of the polymer, χ is Flory's parameter, k_b is the Boltzman constant, T is the temperature. V_0 , n_p and v_c are the standard volume of the gel, the total number of chains in the gel and the molar volume of the solvent, respectively. The osmotic pressure in turn affects the volume of the hydrogel. The change in the hydrogel volume is characterized as the swelling ratio by comparing the dimensions of the hydrogel above and below the LCST. The swelling ratio can be quantified by volume,^{28,29} length,²³ and by weight.^{30,31} The swelling ratio of PNIPAAm ranges from 7 times the shrunken weight,³¹ 4 times the hydrogel film thickness,⁴⁷ a 27% volume change,⁴⁸ etc. The swelling ratio is very dependent on the composition,^{17,49} crosslinker density, curing method and curing time. The reversible nature of PNIPAAm actuation allows for cyclic usage without macroscopic damage.

1.2.3 Light scattering by particles and localized surface plasmon resonance

The interaction between light and small particles was explained based on the electric dipole concept in 1871 by Lord Rayleigh. In 1908, Gustav Mie explained the scattering of light by spherical structures through Maxwell's electromagnetic theory.⁵⁰ The orange skies at dawn and dusk and the blue skies at noon can be explained by Rayleigh scattering while the white color of clouds is explained by Mie scattering. Mie scattering also helps explain localized surface plasmon resonance (LSPR).

Particles of noble metals, whose sizes are comparable to the incident light wavelength, interact with light by Mie scattering. The light absorbed by the particle excites the free electrons. The collective oscillation of free surface electrons in a noble metal is called a plasmon.⁵¹ Plasmon oscillations can be likened to mechanical oscillations of an electron gas with respect to the fixed ionic cores of a metal. At the metal surface, plasmons are called surface plasmon polaritons or simply surface plasmons which can be optically excited. When surface plasmons are confined to a particle whose size is comparable to the wavelength of light, the free electrons collectively oscillate exhibiting LSPR (

Figure 7). As a result of LSPR, the electric fields near the particle's surface are enhanced and the optical extinction of the particle is the highest at its plasmon resonance frequency. For noble metal nanoparticles, the plasmon resonance frequency is in the visible range.⁵¹

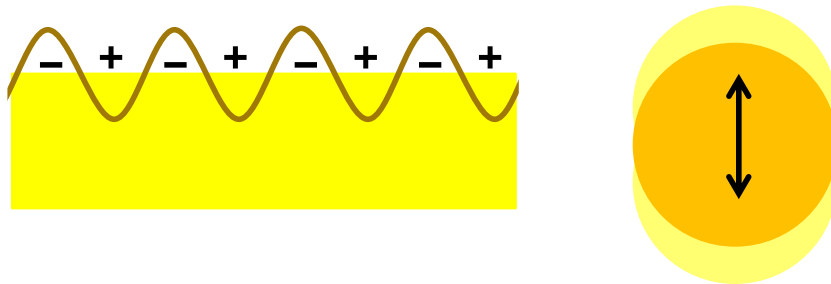


Figure 7: Illustration of surface plasmons (a) and a localized surface plasmon (b)⁵¹

Mie theory, the analytical solution to Maxwell's theory,⁵² calculates the scattering and absorption due to spherical particles. In nanoparticles, the coherent oscillation of conduction electrons is caused by the oscillation of the electric field.^{51,53,54} The incident light is either scattered or absorbed by the particles. The extinction cross section (σ_{Ext}) is

equal to the sum of absorption (σ_{Abs}) and scattering cross sections (σ_{Sca}) as seen in Equation 2.

$$\sigma_{Ext} = \sigma_{Abs} + \sigma_{Sca}$$

Equation 2: Extinction cross section for nanoparticles

Gold nanoparticles are widely studied due to their unique properties of surface plasmon resonance, plasmon absorption, surface enhanced Raman scattering and resonance Rayleigh scattering.⁵⁵ The varying colors of colloidal Au NPs (Figure 8) can be attributed to the particle size, shape, stage of coagulation and composition.^{53,54} Due to LSPR, each nanoparticle has an associated characteristic maximum absorption wavelength based on the particle size. The maximum absorption (excitation) wavelength also depends on the particle size, shape and inter-particle distance.⁴⁴ For example; the excitation wavelength for 20 nm particles is 521 nm and for 40 nm particles, the excitation wavelength is 532 nm.

$$\lambda_{max} = 515.04 + 0.3647d$$

Equation 3: Relationship between the wavelength of the incident light and the diameter of gold nanoparticles.⁵⁵

where d is the diameter in nanometers. This equation relates the excitation wavelength to the particle size. This has a regression value of 0.9902. Figure 8 shows the relationship between particle size and color of the colloidal solution.



Figure 8: Photograph showing the color of colloidal gold based on particle size⁵⁶

From the available gold nanoparticle shapes (rods, urchins, wires, shells, triangles, stars, cubes, etc), gold nanospheres were selected for this project due to their uniformity. If nanorods had been chosen, the fabrication method would not allow control of the orientation of rods in the sample. Therefore, nanospheres were used. The size of the nanosphere used was determined based on the wavelength of the available light source (532 nm, green light).

1.2.4 General characterization and fabrication methods

GOLD PARTICLE CHARACTERIZATION METHODS

Gold nanoparticles were characterized by ultra violet-visible spectrophotometry (UV-Vis), dynamic light scattering (DLS) and scanning electron microscopy (SEM). In Ultra Violet-Visible (UV-Vis) spectrophotometry, light in the ultra violet and visible wavelengths (100 nm – 700 nm) is passed through the sample. The difference in light intensity is recorded from which absorption, reflectance and transmission plots can be obtained. In DLS, the fluctuations in the intensity of scattered light as it passes through the colloidal solution are recorded. The particle size is calculated from the fluctuations.⁵⁷ The radius of the particles is typically obtained from the intensity distribution. Scanning

Electron Microscopy (SEM) utilizes a narrow electron beam to image the surface of the samples.

P μ SL PRINTING OF SAMPLES

As an alternative sample fabrication method, the Projection Micro-Stereo Lithography (P μ SL) was explored. An image is projected through the lens and microscopic 3D features can be printed. Blue light is used to cure the samples with the P μ SL. Ultra violet light was used for curing most of the samples fabricated in this project.

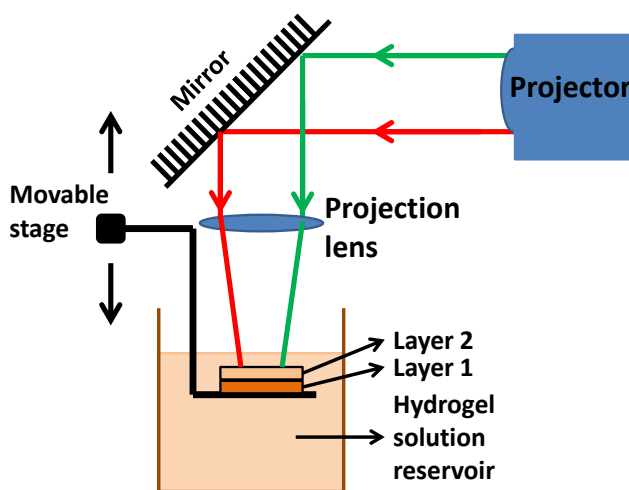


Figure 9: Schematic of the working of the P μ SL. The image of the sample to be printed is projected on the stage.

In P μ SL, the stage is positioned just below the surface of the precursor solution reservoir and the image of the item to be printed is projected. The layer of liquid on which the light is incident is cured. The stage then moves downwards (into the precursor reservoir) allowing for the next layer to be printed (cured). Layer thickness is controlled by the distance between the stage and the surface of the liquid. Adding photoabsorbers can help control the layer thickness and is especially useful when printing features with non-

uniform cross sections. The entire sample can be printed layer by layer with adjustable curing times for each layer. Through P μ SL, micrometer scale structures with uniform and non uniform cross sections can be easily printed in a matter of minutes. The P μ SL uses blue light to cure the polymer solution (see Figure 9). The solution recipe for blue light curing and the UV light curing is different and is described in Section 2.1.3.

1.3 Novelty: Combining the ingredients

In this project, the thermo-responsiveness of the PNIPAAm hydrogel is combined with the photo-responsiveness of the gold nanoparticles to create a phototropic system. This approach allows photo-thermal responsiveness of the system to be tuned by adjusting the concentration of the gold particles and the intensity of the incident light. This project aims to evaluate a new material as a candidate for a phototropic system. The inherent requirement with hydrogel samples is immersion in water and this is crucial to the working of the system.

The hydrogel is transparent and the addition of Au NPs causes a slight red tinge. When light is incident on the sample, it passes through the hydrogel and interacts with the Au NPs in its path. The Au NPs absorb the light and generate heat through plasmon resonance which is transferred to the surrounding hydrogel. When the heat generated rises the temperature to more than 32°C, the hydrogel starts to shrink. Bending of the sample is achieved by differential shrinking across the cross section. The part closest to the light shrinks the most while the part away from the light shrinks the least. This difference in the shrinking causes the sample to bend.

Chapter 2: METHODOLOGY AND EXPERIMENTATION

2.1 Materials

The chemicals, instruments, recipes, and softwares used in this project are listed below along with the company from which the chemicals were purchased.

2.1.1 Chemicals

- Sigma Aldrich: N-isopropylacrylamide (NIPAAm) used as the monomer, N,N'-methylenebis(acrylamide) (BIS) used as the crosslinker, 2-Hydroxy-2-methylpropiophenone (Darocur) used as the UV light photoinitiator, Phenylbis(2,4,6-trimethylbenzoyl)phosphine oxide (Irgacure 819) used as the blue light photoinitiator. Trisodium citrate and gold chloride, used to prepare the Au NPs in lab, were obtained from Sigma Aldrich. The chemical 3(trimethoxysilyl)propyl methacrylate (TPM) was used to treat glass slides and silicon (Si) wafers to chemically bond the hydrogel to the substrate.
- VWR International: Dimethyl sulfoxide (DMSO) used as the solvent and ethanol (200 proof) used for washing and substrate treatment.
- Cytodiagnosics: Gold nanoparticles 40 nm in diameter
- Dow Corning: Sylgard 184 Silicone Elastomer kit used to make molds

2.1.2 Instruments

- Optical microscope: A Leica DM5000 B upright microscope was used to obtain images for the swelling ratio tests.

- UV-Vis spectrophotometer: A Perkin Elmer Lambda 950 S spectrophotometer was used to obtain absorption spectra.
- Plasma Cleaner: Expanded Plasma Cleaner PDC – 001/002 with a 29.6 W RF power setting was used for cleaning the substrates before silanization.
- Westinghouse: 15 Watt green LED outdoor flood lamp used for macro-sample actuation.
- Moodlites: 90 Watt green halogen lamp used for macro-sample actuation.
- Coherent.Inc: A 532 nm, up to 1 Watt variable power class IV Genesis MX STM-Series continuous wave laser from Coherent Inc. was the illumination source.
- Vialux: Industrial grade DLP projector STAR 07 (462 nm) was used in the PμSL printing system.
- Dymax 5000-EC UV- Curing flood lamp with 225mW/cm² power used to cure hydrogel samples.
- Fisher Scientific: A Hamilton™ Kel-F Hub Blunt Point Needle was used to make the Polydimethylsiloxane (PDMS) mold for the sample.

2.1.3 Recipes

- NIPAAm purification: Prior to usage, 50 g of NIPAAm was dissolved in 600 mL of hexane in a round bottomed flask placed in a hot water bath at 80°C. Once the NIPAAm was dissolved, the flask was immersed into an ice bath until the NIPAAm recrystallized. It is then filtered with a Buchner funnel and the purified NIPAAm was dried in an oven at 30°C for a day to evaporate any remaining hexane. This increased the purity of NIPAAm from 97% to 99.9%.

- UV light curing system (used for all samples cast in molds): 400 mg of NIPAAm, 20 mg of BIS and 5 μ L of Darocur were dissolved in 1mL of DMSO. The solution was sonicated to ensure complete dissolution and the vials were wrapped in aluminum foil prior to storage to prevent ambient light induced curing. After sample fabrication, it was immersed in water to replace the DMSO in the sample. The sample changes from opaque to transparent when the DMSO has been replaced.
- Blue light (462 nm) curing system (used for P μ SL printing): 400 mg of NIPAAm, 20 mg of BIS, 15.2 mg of Irgacure 819 dissolved in 1 ml of DMSO. The solution was sonicated to ensure complete dissolution and vials were wrapped in aluminum foil prior to storage to prevent ambient light induced curing. After sample fabrication, it was immersed in water to replace the DMSO in the sample. The sample changes from opaque to transparent when the DMSO has been replaced.
- Lab fabricated Au NPs: The sodium citrate reduction method was used where 300 mL of 0.5 mM gold chloride is heated in a beaker with a stir bar. Once the gold chloride solution starts boiling vigorously, the solution was stirred at 900 RPM and 30 mL of 38.8mM trisodium citrate solution was added. The solution first turns colorless and then starts turning dark. After 15 – 20 minutes of adding the trisodium citrate solution, the reaction is complete. The aim was to fabricate uniform particles of 40 nm diameter.
- Pre-treatment of Au NPs from Cytodiagnostics: Prior to usage, the Au NPs suspended in a phosphate buffered saline were centrifuged for 10 minutes at 14,800 rpm and the supernatant was removed. Deionized (DI) water was added and centrifuged again at

the same speed for 10 minutes. The water was removed and the Au NPs were introduced into the hydrogel solution.

- PDMS molds: A 1:10 ratio by weight of curing agent to the silicone elastomer from the Sylgard 184 elastomer kit was mixed and degassed before being poured on the master. Molds were cured at 70°C for three hours.
- Silanization treatment of substrate: A bath of 200 mL of ethanol with 1 mL of TPM was prepared. Just before oxygen plasma treated substrates were immersed, 6 mL of 10% by volume acetic acid was added. The substrates were immersed for a minimum of two hours. To terminate the treatment, the substrates were triple washed in ethanol and dried. The silanization treatment lasts up to two weeks for glass slides and up to a week for Si wafers.

2.1.4 Softwares

- Measurements from images were obtained through ImageJ
- The data was plotted using Origin

2.2 Experimental procedure

The experimental section is divided into two main parts; preliminary background study—where the hydrogel and Au NPs were characterized—and focused study, where samples were illuminated with a laser source and actuated. First the background study will be presented followed by the focused study experiments.

2.2.1 Background Study

This experimental section focuses on establishing and characterizing the basic properties of the Au NPs used in the system as well as preliminary swelling ratio information for the PNIPAAm. Au NPs were prepared in lab and characterized by DLS, UV-Visible spectrophotometer and SEM to obtain and confirm the particle size.

SYNTHESIZING Au NPS IN THE LAB

The goal was to fabricate Au particles 40 nanometers in diameter to correspond to the wavelength of the laser (532 nm) in the lab. Six batches of Au NPs were prepared with different stirring times of 10 minutes, 20 minutes, 25 minutes and 30 minutes (with the standard recipe listed in Section 2.1). Trials with 1/5th the regular trisodium citrate concentration and half the regular trisodium citrate concentration were also conducted with the solution being stirred for 15 minutes (see Table 5). Lowering the trisodium citrate concentrations would help grow larger particles.

PμSL SAMPLE FABRICATION

As an alternative to using PDMS molds for sample fabrication, 3D printing of the sample through PμSL was explored. Cubes of 150 μm on each side with varying amounts of Au NPs were printed on TPM treated silicon wafers which were used for constrained ratio testing described below.

SWELLING RATIO TESTS: LOW Au NP CONCENTRATIONS

Cooling curve swelling ratio tests were carried out to quantify the change in length for our specific system. This would give insight into the bending angle for the final sample. Cooling curve swelling ratio refers to data collected as the sample temperature drops. This differs from heating curve swelling ratios where data is collected as the sample temperature rises. Both constrained and unconstrained samples were tested. Constrained here, refers to the sample being chemically bonded to a silanized substrate. These samples were printed by the P μ SL. Unconstrained samples were cast in a PDMS mold and allowed to swell in water. The 4 cm x 1 cm x 1 mm samples were cut into small cubes about 1 mm x 1 mm x 1 mm by a razor blade. Both constrained and unconstrained tests were carried out in a water bath setup under the microscope. The change in length was recorded and analyzed over the cooling curve while being submerged in water. Due to the proximity to the sample, the water temperature is assumed to be the sample temperature.

For the constrained tests, the silanized Si wafer with the constrained sample was submerged in a small petridish with room temperature water. This petridish was placed in a bigger petridish forming a water bath. The bigger petridish was placed under the microscope (see Figure 10). The orange putty was used to stop the small petridish from floating around. The blue putty held the thermocouple down. Hot water (above 70°C) was added to the outer petridish and images were taken at every degree from 42°C till 18°C as the water cooled down. The temperature was measured through a thermocouple placed in close proximity to the sample.

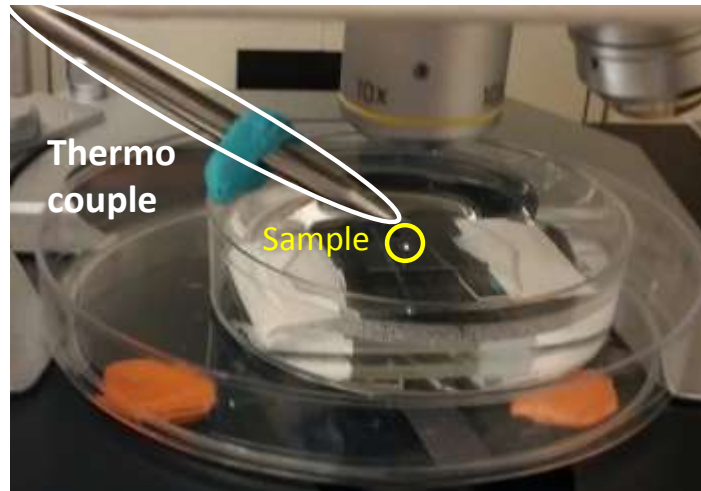


Figure 10: Photograph of the setup for constrained cooling curve swelling ratio tests.

For the unconstrained swelling ratio tests, the sample moved around in the petridish. Again, a water bath design was used and a thermocouple recorded the water temperature. Hot water was introduced in to the petridish surrounding the water bath. Data was collected from $42^{\circ}\text{C} - 18^{\circ}\text{C}$ as the water cooled down.

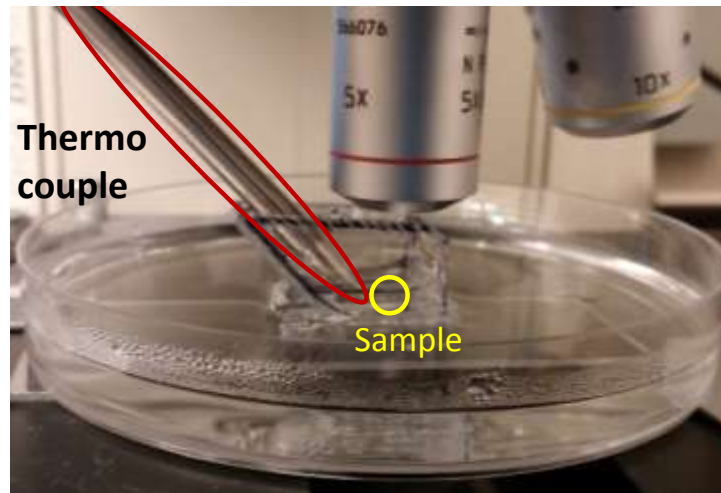


Figure 11: Photograph of the setup for the unconstrained swelling ratio tests

Constrained and unconstrained swelling ratio tests were carried out on samples with 0 ml of Au NP/ml of hydrogel (pure hydrogel), 0.1 ml of Au NP/ml of hydrogel (referred to as 0.1x), 0.2 ml of Au NP/ml of hydrogel (referred to as 0.2x) and 0.3 ml of Au NP/ml of hydrogel (referred to as 0.3x). The Au NPs used for these tests were not pre-treated as described in Section 2.1.3. The data from these swelling ratio tests will be used correlate the extent of bending in further tests.

Table 1: Conversion between a volume based and absolute Au concentration in the system

Volumetric	0x	0.1x	0.2x	0.3x	0.8x	10x	20x
Absolute ($\mu\text{g/mL}$)	0	4.65	9.30	13.95	37.2	465	930

MACRO-SAMPLE TESTING: HALOGEN AND LED LAMPS

Simultaneously, macro samples with multiple layers—each layer with a different concentration of Au NP—were also fabricated and tested with a 90 W green halogen lamp. The samples were fabricated in PDMS molds (Figure 12). The samples were suspended in a beaker with degassed DI water and illuminated by the halogen lamp at a 90° incident angle. The first layer was cured for 10 seconds. On top of this layer, the second layer precursor solution was added and cured again for 10 seconds. The last layer was cured for 20 seconds to ensure complete curing of the sample. The bottom layer was cured for the longest time since the layers were transparent and allowed the UV curing light to penetrate all the way through to the bottom. Based on the volume of the PDMS mold in the PDMS:Glass slide method, a sample could have only three layers.

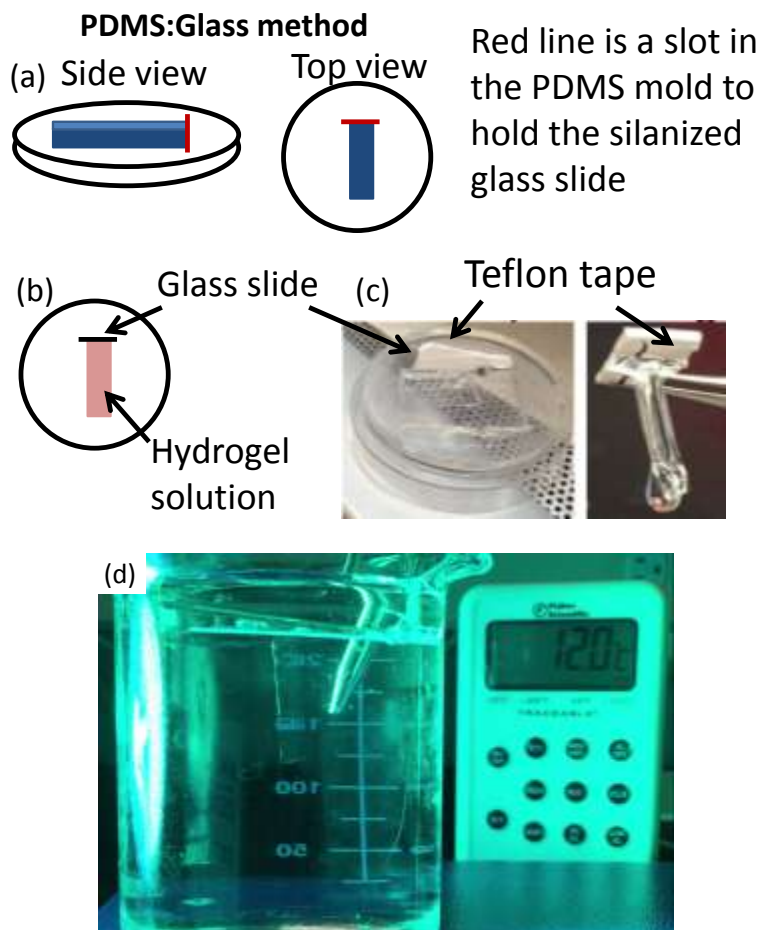


Figure 12: Schematic showing the PDMS:Glass slide method in which the silanized glass slide placed in the slot in (a) adheres to the hydrogel solution introduced in (b). Photograph of the final sample (c) and the test setup for macro-samples (d).

Five types of macro-samples were tested with the green halogen lamp six inches away. The sample temperatures were measured using a thermocouple in a beaker of water. The tests started at 12°C in degassed water and the lamp was turned off when the sample reached 40°C. Video recording of the tests were done till the samples cooled down till 30°C.

Table 2: Composition of the macro-samples used for testing with halogen and LED lamps

Sl. No	Sample type	Layer volume (μL)	Composition (bottom layer to top layer)
1	Gradient	120, 40, 40, 40	0x, 0.1x, 0.2x, 0.3x
2	Anti-gradient	120, 40, 40, 40	0.3x, 0.2x, 0.1x, 0x
3	Double gradient	120, 40, 120	0.8x, 0x, 0.8x
4	Pure hydrogel	200	0x
5	Constant concentration	200	0.2x

After being illuminated by a halogen lamp, the samples listed in Table 2 were also illuminated with a 15W green LED lamp. The results for both halogen and LED lamp illuminated are listed in Section 3.1. A literature search to compare the light intensities and Au NP concentrations was conducted. The results in Table 3 compare light intensities and Au concentrations in different systems.

Table 3: Comparative study of light intensities and Au NP concentrations

Sl. No.	Power density (mW/cm^2)	Mass of heat generator /Mass of NIPAAm (mg/mg)	Sample size (μm)	Reaction time scale (minute)	Sample shape
1	1100	2.5	100 – 200	4 – 20	Cubes or strands ⁵⁸
2	1600	6×10^{-5}	200	40	Microfluidic valve ⁵⁹
3	3	1.5	0.5		Spheres ⁶⁰
4	10	2.16×10^{-2}	0.3	6	Spheres ⁶¹
5	800	1130	$0.05 \times 0.01 \times 1000$	3	Cuboid ⁶²
6	41.8	2.65×10^{-2}	$650 \times 100 \times 90$	1	Cuboid ⁶³
7	24.5 – 66.1	3.5×10^{-2}	1000 x 4000 x 200	40 – 60	Cuboid
8	12658.23 – 63192.14	$1.16 \times 10^{-3} - 2.3 \times 10^{-2}$	1400 x 8100	0.17 – 2	Cylinder (diameter x height)

From Table 3, rows 1 – 4 are values from papers that use gold nanoparticles with the NIPAAm. Rows 5 and 6 (*italicized*) are systems that use graphene oxide and magnetite nanoparticles as the heat generators. They are included in the comparison table since those papers achieve bilayer actuation in a way similar to our approach. Row 7 has the intensities of the halogen and LED lamps used with the macro-samples. The macro-samples use a much lower gold concentration and lower intensity of light than the other cases presented. The intensity of the light source was calculated by dividing the power by the spot size of the light source 6 inches away. The gold content was calculated based on the amount of Au NP solution used in the samples. Row 8 has laser intensities used to test the cylindrical samples used in the focused study. These samples use a higher gold concentration and higher intensity of light.

2.2.2 Focused Study

The focused study builds based on the results from the background study. Cylindrical samples with a higher concentration of Au NPs were fabricated and actuated with higher intensity light. The cylinders have a hydrogel base which was chemically bonded to a silanized glass slide.

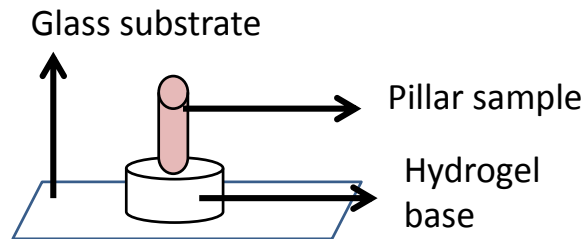


Figure 13: Design of the pillar sample used for bending angle and variable angle tests

The Au NPs used for experiments in the focused study were all rinsed once in DI water and only the nanoparticles (and no solution) were incorporated with the hydrogel. The sample with 10 ml of Au NP/ml of hydrogel has 4.56 μg of gold and is referred to as the 10x sample. The sample with 20 ml of Au NP/ml of hydrogel has 9.12 μg of gold and is referred to as the 20x sample. The weight of gold in the sample is calculated based on the volume of the pillar, the concentration of gold nanoparticles and the particle size. The samples for all tests in this section were submerged in DI water.

SWELLING RATIO TESTS: HIGH Au NP CONCENTRATIONS

Unconstrained swelling ratio tests were conducted to quantify the swelling of the samples in response to both heat and light. Again, the swelling ratio tests were conducted in a water bath (see Figure 11) and hot water was added. The samples for the swelling ratio tests were cut from a bulk 10x and 20x hydrogel sample with a razor. For the light induced swelling ratio tests, the 532 nm laser at 400 mW illuminated the sample as data was recorded through the microscope it was under (see Figure 14). Heat produced by the Au NPs raised the temperature of the hydrogel around it.

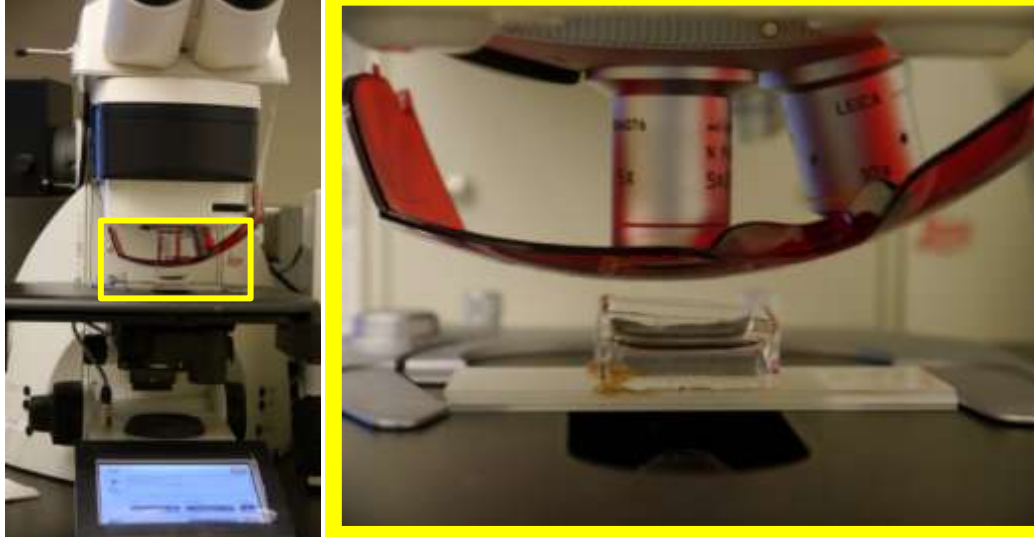


Figure 14: Setup for the laser induced swelling ratio tests. The red glasses are laser protective and prevent the microscope CCD from saturating.

BENDING ANGLE TESTS

Bending angle tests were carried out to quantify the degree of bending and its dependence on laser intensity (power). Both the 10x and the 20x samples were illuminated by a 532 nm laser for two minutes with a 90° incident angle. Images from the video recorded were analyzed to obtain the bending angle at each time step. For the bending angle tests, samples were placed in a glass case with water directly in front of the laser.

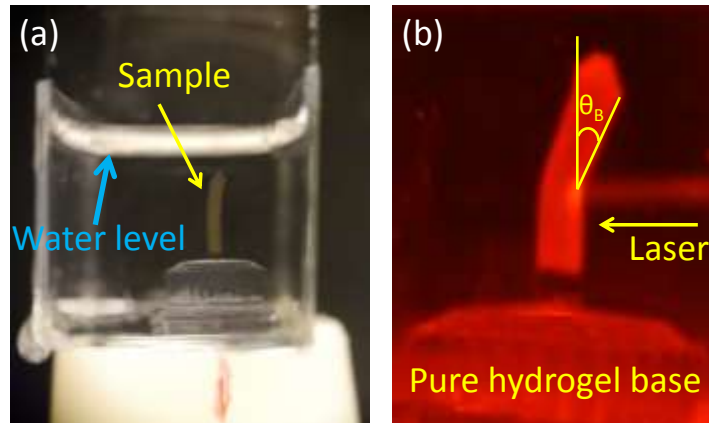


Figure 15: Photographs of the sample in the glass case. (a) The laser comes in from the right. Overlay in (b) shows the measurement of the bending angle (θ_B). The image appears red since laser protective red glasses were placed in front of the camera.

Figure 15a shows the sample in ambient light. The sample in Figure 15b is red because of the laser-protective red glasses placed in front of the camera to stop the charged coupled device (CCD) in the camera from saturating. While performing experiments, the same glasses were worn to protect eyes from the laser. Henceforth, the laser intensities are referred to by their powers (100 mW – 500 mW).

Table 4: Calculated intensities for the laser powers used in experiments

Laser Power (mW)	Intensity (mW/cm ²)
100	12658.23
200	25316.46
300	37974.68
400	50632.91
500	63291.13

VARIABLE ANGLE TESTS

For a system to be considered phototropic, its response to light incident at an angle is to be measured. Variable angle tests were carried out to measure the phototropic response.

The 10x and the 20x samples were illuminated for two minutes at a 400 mW laser power.

For the variable angle tests, a mirror was used to deflect the laser beam.

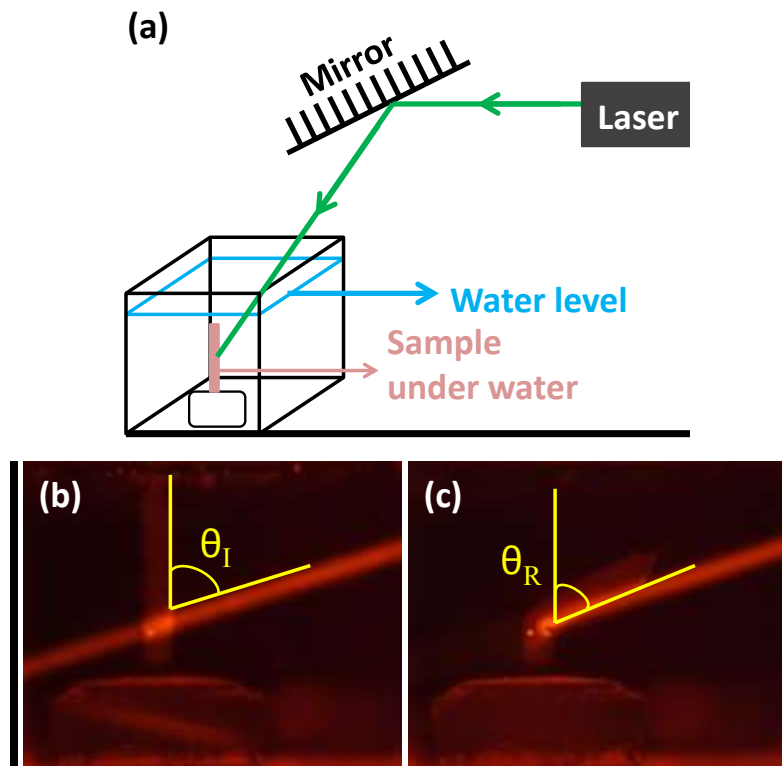


Figure 16: Schematic for the variable angle testing (a). Photograph of the samples illuminated with laser overlaid with the measurements of the incident angle θ_I (b) and the response angle θ_R (c).

Chapter 3: RESULTS AND DISCUSSION

3.1 Background Study

As part of the background study, hydrogel and the nanoparticles were utilized to understand relevant properties and behavior. The results of characterizing the Au NPs and the hydrogel are discussed below.

3.1.1 Characterization of Au NPs with varying stirring times

The six batches of Au NPs fabricated in the lab were characterized to obtain the particle size. Table 5 summarizes the particle size and Figure 17 outlines the particle sizes obtained from characterizing the batches prepared in our lab. The batches were characterized by comparing UV-Vis measurements taken to literature measurements^{52,55,64,65} and by plugging the maximum absorption wavelength in Equation 3. The wavelengths corresponding to the peaks in the UV-Vis absorption spectra were compared to literature sources. For batches with different stirring times, the particle sizes were obtained from UV-Vis measurements. Lowering the stirring timings would allow the Au atoms to agglomerate at the existing nucleation sites and form larger particles.

Table 5: Au NP batches with varying stirring times along with their particle sizes

Batch	Stirring time (minute)	UV-Vis Diameter (nm) Literature based ^{52,55,64,65}	UV-Vis Diameter (nm) calculated from Equation 3
1	10	13 – 20	16.43
2	20	9 – 15	2.63
3	25	21 – 25	13.6
4	30	10 – 20	13.6

UV-Vis SPECTROPHOTOMETER CHARACTERIZATION

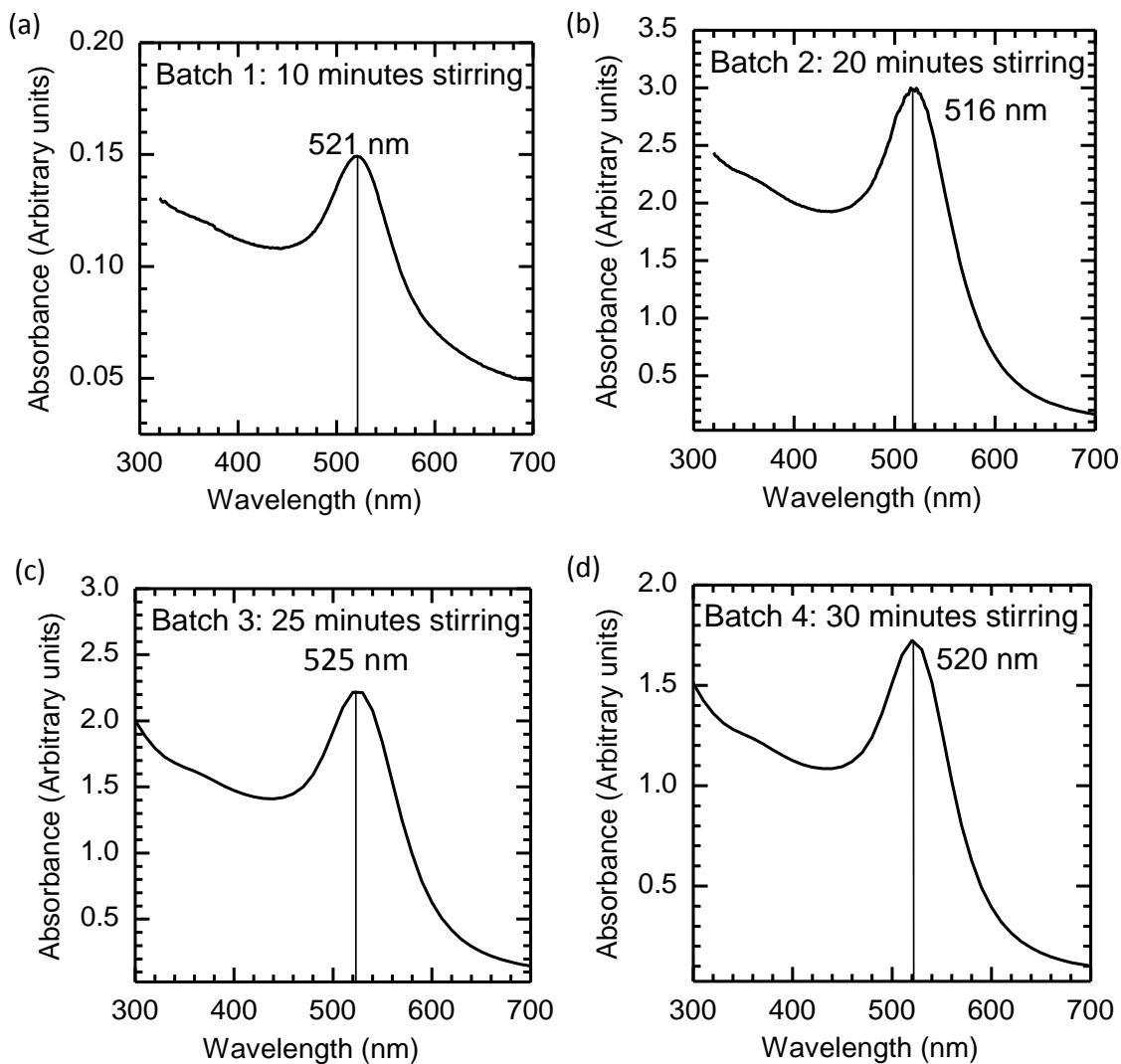


Figure 17: UV-Vis spectrophotometer absorption curves for the first four batches of particles prepared. They were stirred for 10 minutes (a), 20 minutes (b), 25 minutes (c) and 30 minutes (d). The particle size is unaffected by different stirring times.

The UV-Vis absorption spectra show the peak absorption of the incident light. Based on the analysis of batches 1 – 4, the absorption peak is not close to 532 nm. Consequently, the particle diameter is not close to 40 nm. Peaks closer to 520 nm indicate at particle sizes closer to 20 nm.

3.1.2 Characterization of Au NPs with varying reducing agents

To increase the Au NP size, less of the reducing agent; sodium citrate was added allowing the gold atoms in solution to grow more once nucleation began as there are fewer nucleation sites. Evidence of increased particle size was found through SEM, UV-Vis and DLS analysis (see Table 6).

Table 6: Summary of Au NP sizes for batches with lower trisodium citrate

Batch	Citrate concentration	UV-Vis Diameter (nm) Literature based ^{52,55,64,65}	UV-Vis Diameter (nm) Based on Equation 3	SEM Diameter (nm) (Standard deviation)	DLS Diameter (nm)
1	0.2 x	40 – 70	93.12	60.34 (15.29)	117 – 174
2	0.5 x	10 – 20	19.08	64.88 (1.62)	29 – 65

There is an increase in the particle size between the first four batches and the two batches with lower sodium citrate concentration. Despite the number of characterization methods used, a conclusive estimate of the particle size could not be obtained.

UV-Vis SPECTROPHOTOMETER CHARACTERIZATION

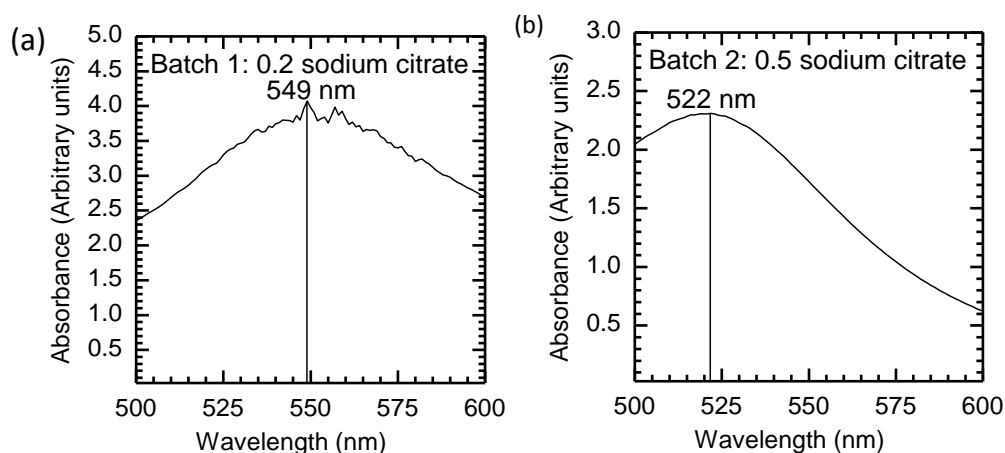


Figure 18: UV-Vis spectrophotometer absorption graphs of the last two batches with one fifth the sodium citrate amount (a) and half the sodium citrate amount (b).

UV-Vis spectrophotometer scans show greatest absorption at 549 nm and 522 nm. This corresponds to a particle size of about 93 nm and 19 nm for batches 1 and 2, respectively. Though both these wavelengths are green, the target absorption wavelength of 532 nm was not achieved. SEM analysis was carried out for further characterization of the particle size.

SCANNING ELECTRON MICROSCOPY IMAGING AND ANALYSIS

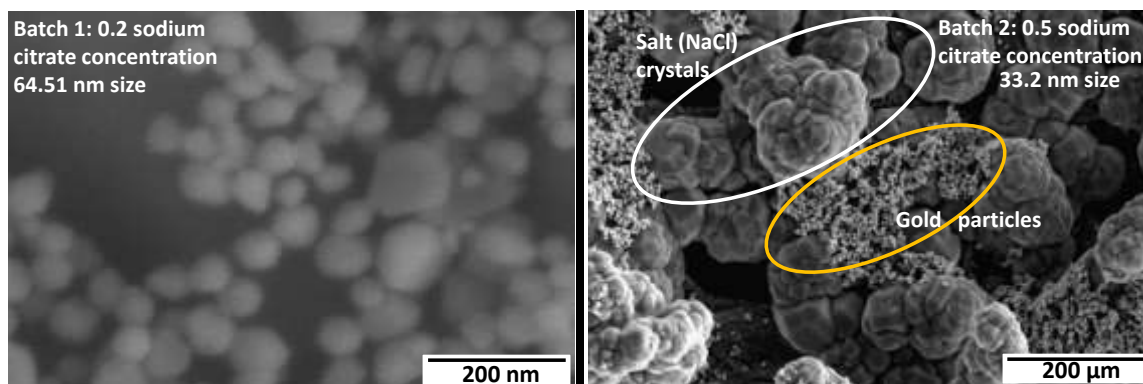


Figure 19: SEM images of gold nanoparticles fabricated in the lab. Image on the right shows NaCl crystals in the sample despite being twice rinsed in DI water.

While SEM imaging and analysis gave an average size, it was discordant with the other measurements/calculations obtained. Fifty seven measurements were taken through the SEM images and averaged to obtain the particle size for each SEM image. Batch 1 with its particle size of 60.34 nm has a standard deviation of 15.29 nm and Batch 2 with a particle size of 64.88 nm has a standard deviation of 1.62 nm.

DYNAMIC LIGHT SCATTERING ANALYSIS

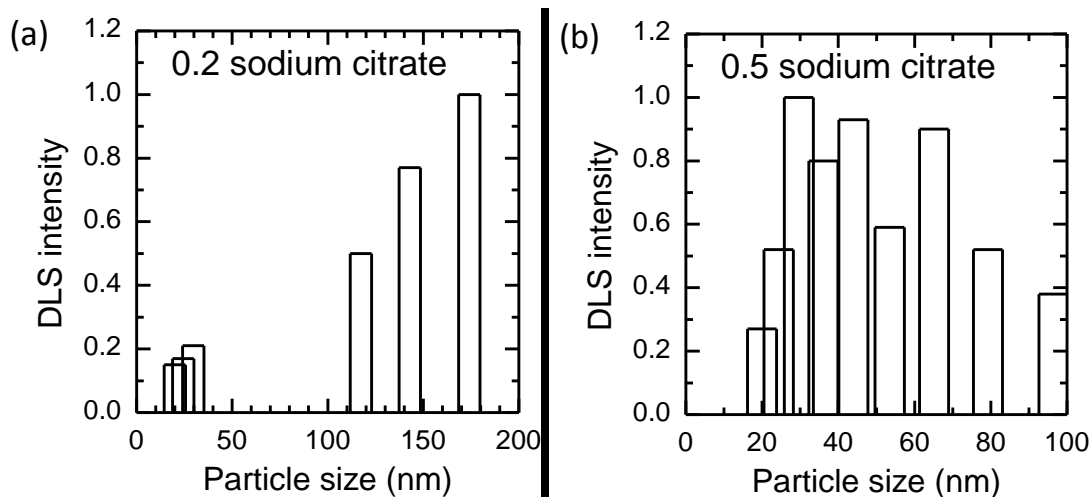


Figure 20: DLS results showing the particle diameter of the gold nanoparticles.

The DLS intensity plots show high intensity of scattered light corresponding to the particle diameter. From Figure 20a, highest intensity was seen when the particle size was around 175 nm. In Figure 20b, the particle size 30 – 65 nm.

The calculated, measured and extrapolated diameters show that adding less of the reducing agent leads to particles of higher diameter. However, a conclusive estimate of the size could not be obtained from the results as different methods gave different diameters. It was this variation in the particle size which called for buying the particles to ensure uniformity of the particle size in the system. Exploring the Au NP synthesis methods would cost time.

3.1.3 Swelling ratio tests: Low Au NP concentration samples

To characterize the hydrogel's response to thermal stimulus, cooling curve swelling ratio tests were conducted. The samples were either constrained (attached to a silanized

substrate) or unconstrained. Cooling and not heating curve tests were conducted due to the equipment limitations and challenges of not having a temperature controlled setup. The water bath design was utilized for three reasons. First, adding the hot water directly would move the sample. Second, to lower the temperature, ice was added which would cause a disruption in the water causing the image in the microscope to distort. Third, the ice could contaminate and compromise the sample reducing its reusability.

The water added was hotter than 70°C for three reasons; first to increase the temperature of the inner water bath, second to compensate for the heat lost to the ambient air due to a large exposed area and third to allow the sample to equilibrate well before data was collected. Evidence of hysteresis loss in the heating and cooling curves was seen. The swelling ratio at 25°C from the cooling curve is different from the swelling ratio at 25°C from the heating curve. For both the constrained and unconstrained swelling ratio tests, the minimum length is considered as 1 and the data collected is normalized based on this minimum length. The results are summarized in Table 7.

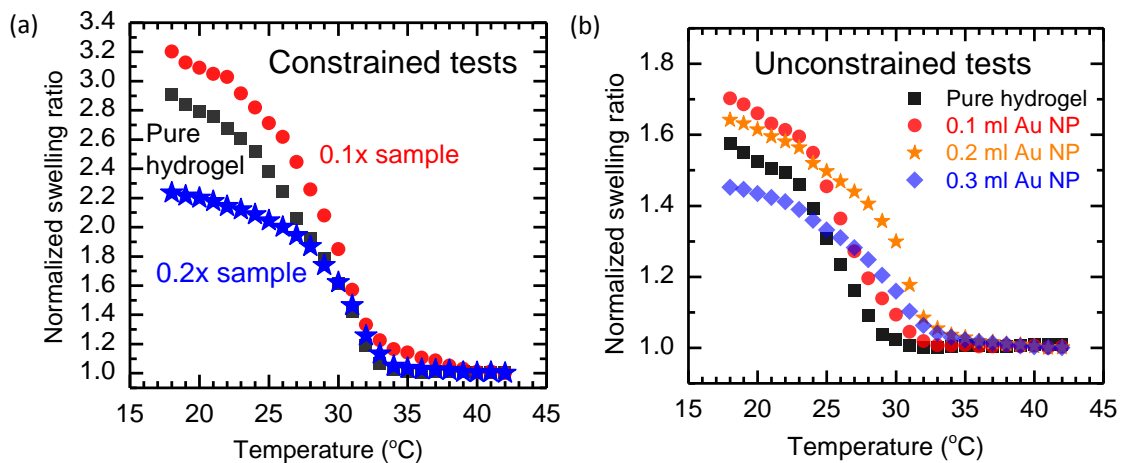


Figure 21: Normalized swelling ratio test results for varying Au NP concentrations

Table 7: Averaged swelling ratios from constrained and unconstrained samples

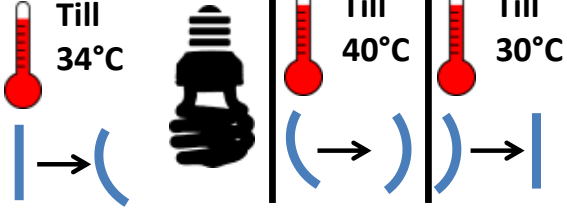
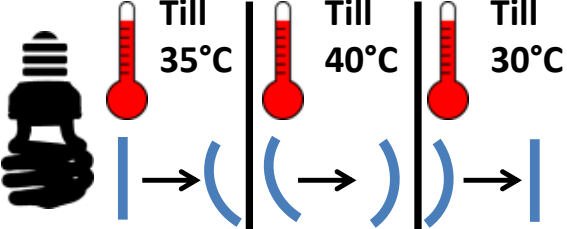
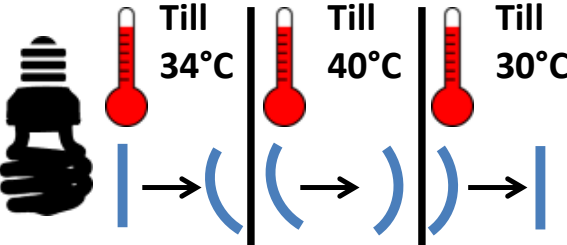
	0	0.1x	0.2x	0.3x
Constrained samples	2.90	3.2	2.23	-
Unconstrained samples	1.57	1.70	1.64	1.45

The 0.3x sample for the constrained test was damaged before tests could be run. P μ SL printing could not be done at that time. From Figure 21a, it appears that except the pure hydrogel curve, increasing the gold concentration decreases the swelling ratio. From Figure 21b, the same trend is seen. The design for the final sample was a cylindrical pillar attached to a silanized glass substrate. This meant the hydrogel at the top of the pillar would behave differently than the hydrogel at the base of the pillar which is bonded chemically to the glass substrate. The constrained tests would give insight to hydrogel behavior at the base while the unconstrained tests would give an idea about the top of the pillar where the bonding with the glass substrate does not affect the hydrogel.

Simultaneously, experiments on rectangular macro-samples made by the PDMS:Glass method (Figure 12d) were conducted with a green halogen lamp which was placed six inches away. The samples were cast in a PDMS mold and attached to a silanized glass slide (Figure 12). The illumination direction is important because the top layer of the sample (cured for 20 s) was always facing the light. This meant that the bottom layer that was cured the most was away from the light/heat source.

Table 8: Summary of the macro-sample test results illuminated with the halogen lamp

Sl. No	Sample type	Composition (top to bottom/closest to light to farthest from light)	Temperature range (°C)	Illumination direction	Results
1	Gradient	0.3x, 0.2x, 0.1x, 0x	12 – 40 – 30	Left to right	
2	Anti-gradient	0x, 0.1x, 0.2x, 0.3x	12 – 45.6	Left to right	
3	Double gradient	0.8x, 0x, 0.8x	12 – 40 – 30	Left to right	

4	Double gradient	0.8x, 0x, 0.8x	12 – 40 – 30	Right to left	
5	Pure hydrogel	0x	12 – 40 – 30	Left to right	
6	Constant concentration	0.2x	12 – 40 – 30	Left to right	

The macro-sample tests showed that the samples bent preferentially to one direction as seen from samples 1, 2, 3 and 4. From samples 1 and 2, it is evident that despite a compositional difference, the behavior of the samples does not change. If the bending were photo-thermally driven, the presence of and gradient in the Au NPs should affect the direction of bending. In samples 3 and 4, the same behavior is expected because the sample is compositionally symmetrical (0.8x, 0x, 0.8x). Here, a difference in the behaviors is seen even with the same sample. To further demonstrate this behavior, samples with no Au NPs and a constant concentration of Au NPs (0.2x) were also illuminated with the halogen lamp. It was noted that the halogen lamp radiated considerable heat which was believed to interfere with the mechanism of the photo-thermally activated system.

To eliminate any interference of heat driven actuation, the samples previously illuminated with a halogen lamp were illuminated with a 15 W green LED lamp also placed six inches away. When exposed to the green LED lamp, none of the samples bent. The LED lamp radiated far less heat. The samples were directly heat actuated rather than the Au NPs converting the incoming light to heat. To further support this point, the samples were also illuminated with the lamp three inches away with no actuation being seen.

The preferential bending was due to the sample preparation method. In the PDMS:Glass slide method, the whole sample was cured layer by layer. The transparent layers allow the UV light to penetrate all the way through the mold curing the bottom layer for cumulatively the longest time. This meant that the bottom layer had maximum

crosslinking making it the stiffest layer. With a softer top layer, when the sample was illuminated, the sample always bent towards the softer layer. The entire structure resembled a bilayer with one layer being stiffer than the other (Figure 22). Regardless of the composition, the bottom layer was always the stiffest (highly crosslinked) layer of the sample.

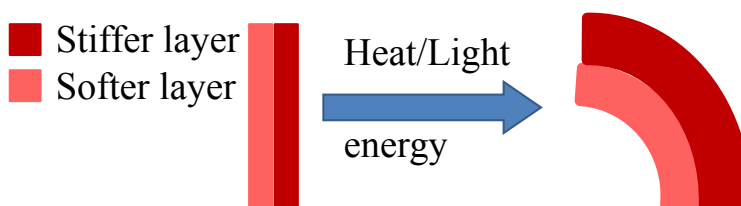


Figure 22: Schematic of a bilayer with different stiffnesses bending in response to stimuli

Based on the results of the halogen and LED lamp tests, further tests were conducted with samples having more Au NPs and a stronger light source was used.

3.2 Focused Study

From the background study, it was clear that obtaining uniformly sized Au NPs was challenging and thus purchasing rather than fabricating the Au NPs would be preferred. An accurate estimate of the particle size could not be determined due to disparity of results from SEM, DLS, UV-Vis measurements and calculations. Preliminary tests with the 0.1x, 0.2x and the 0.3x samples with the halogen lamp was more heat driven than light driven; a fact further supported by the LED tests. The light source was weak and the concentration of the Au NPs was low.

The concentration of the Au NPs in the samples was increased to 10 and 20 times the volume of the hydrogel. The Au NPs from 10 mL of the colloidal solution was rinsed in DI water and added to 1 mL of the hydrogel solution to give the 10x precursor solution. The new more intense light source used was a laser with up to 1W power over a 1 mm diameter spot size. Swelling ratio tests, bending angle tests and variable angle tests were conducted as mentioned in the Experimental section.

3.2.1 Swelling ratio tests: High Au NP concentration samples – Heat actuated

Swelling ratio tests with the high concentration samples were conducted in a way similar to those conducted with the low Au NP concentration samples. Only unconstrained tests were conducted for the high concentration samples. The sample design had changed where now a hydrogel pillar was attached to a hydrogel base. The behavior of the pillar would be similar to unconstrained samples.

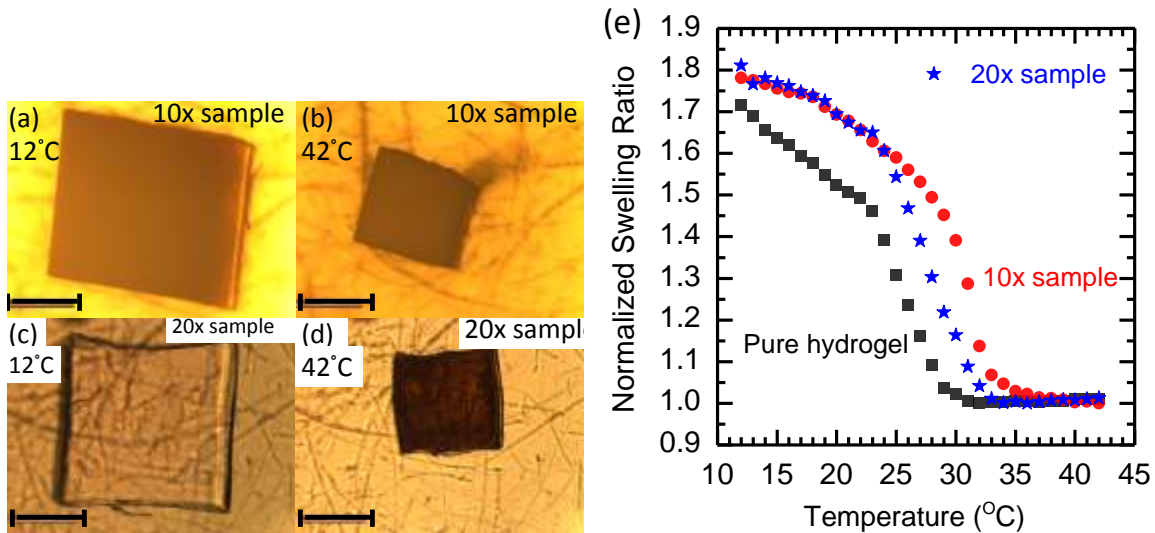


Figure 23: Optical microscope images of the 10x (a), (b) and 20x (c), (d) samples used for the unconstrained swelling ratio tests. Scale bar is 500 μm. Normalized swelling ratio tests of the 10x and 20x samples. Data from the pure hydrogel unconstrained swelling ratio tests is also included for reference.

The swelling ratio for the 10x samples is 1.78 while the ratio for the 20x sample is 1.81. This is comparable to the unconstrained sample swelling ratios from Table 4. There is a visible difference in the swelling ratio of the pure hydrogel, 10x and 20x samples between 25°C – 35°C.

3.2.2 Swelling ratio tests: High Au NP concentration samples – Light actuated

Laser induced swelling ratio tests were conducted. This was done to compare the heat actuated and light actuated swelling ratios. It was expected that the heat and the light induced swelling ratios would be very comparable. The samples were placed under a microscope and the laser at 400 mW power was aimed at the sample. They were illuminated for at least 30 seconds or until the samples shrunk. Due to constraints in the lab, the swelling ratio was obtained by measuring the lengths at room temperature and at a temperature above 32°C. The swelling ratios for the 10x and the 20x samples were 2.41 and 3.37, respectively. It is expected that if the measurements were taken at 12°C, the swelling ratio would be higher.

Table 9: Summary of unconstrained swelling ratio results

Actuator	10x sample	20x sample
Heat	1.78	1.81
Laser	2.41	3.37

The difference in the swelling ratios between the heat and laser actuated trials can be explained by the efficiency of heat generation within the sample. With the heat actuated tests, hot water is added in the water bath. In the laser actuated tests, the samples are illuminated directly and heat generation is more efficient.

3.2.3 Bending angle tests

To map the response to various laser intensities, bending angle tests were conducted where the incident angle was 90° . Powers from 100 mW – 500 mW was used and the samples were illuminated for two minutes. Based on response time, the results were analyzed every ten seconds (10x samples) or every second for the first ten seconds (20x samples) and a reading at 120 s was taken.

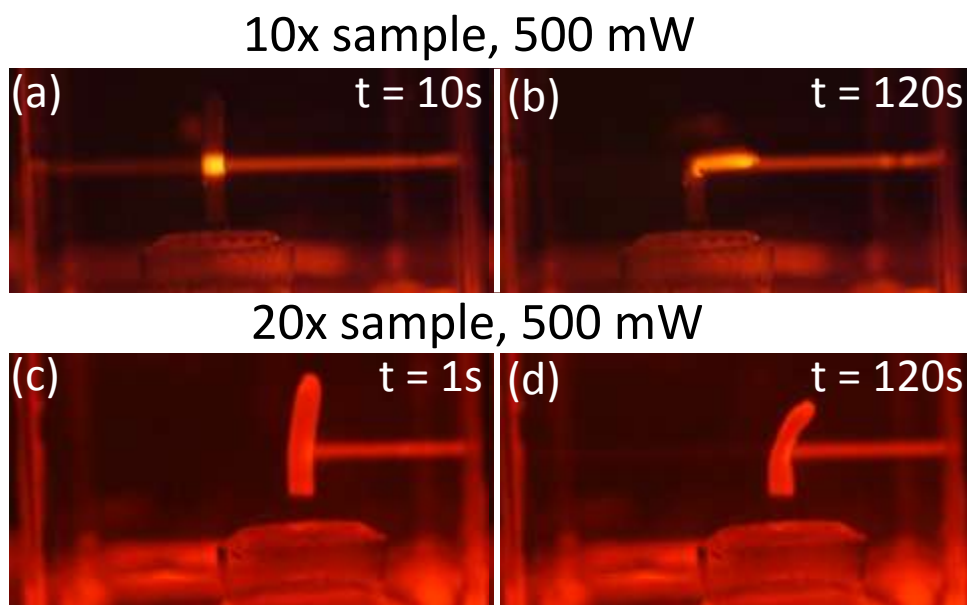


Figure 24: Photographs of the laser actuated bending angle samples. Notice the difference in the intensities before and after it passes through the sample.

Note that the images are taken with the red laser protective glasses and this reduces the intensities recorded in the images. In the 10x sample tests, the laser intensity drops drastically between 10 seconds and 120 seconds. This is because the laser goes through more of the when it is bent than initially. In the 20x sample tests, there is an increase in the laser intensity that passes through the sample. The high concentration of Au NPs in

the sample absorbs most of the light allowing very little to pass through. However, when the sample shrinks reducing its diameter, some light passes through the sample.

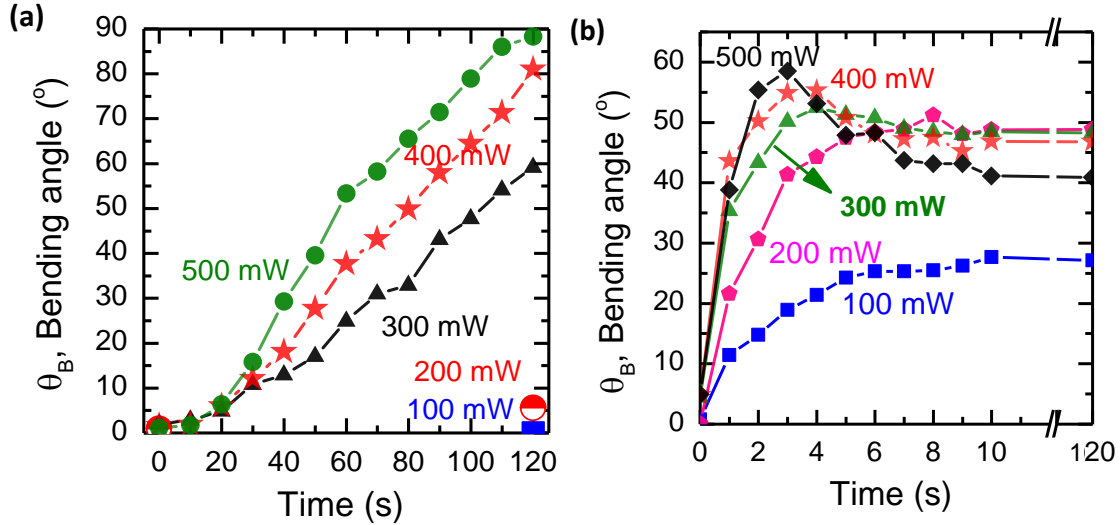


Figure 25: Bending angle vs. time graph for the 10x sample (a) and the 20x sample (b). Note the time scale difference in (a) and (b).

Each point on both plots in Figure 25 is an average of three trials. With 100 mW, the sample actuated 0° whereas for 200 mW, the bending angle was 5.6° . The laser induced heat generation was not sufficient to actuate the sample. With higher intensities or longer times, actuation would occur. Table 10 details the bending angle along with equations for the linear trend lines for trials with 300 mW, 400 mW, and 500 mW.

Table 10: Summary of the trendlines for the 10x sample

Power (mW)	Slope	y intercept	R ² value	Bending angle (°)
300	0.51	-4.03	0.9789	59.15
400	0.70	-5.67	0.9891	80.98
500	0.82	-3.46	0.9808	88.36

Table 11: Change in the bending angle for the 20x sample

Power (mW)	Angle at 4 s	Angle at 10 s	Angle at 120 s
100	21.39	27.67	27.13

200	44.25	48.75	48.80
300	52.44	48.42	48.25
400	55.34	46.82	46.76
500	53.13	41.11	40.89

Within the first 10 seconds of illumination, most of the actuation occurs. Between 10 seconds and 120 seconds, there is not a large change in the bending angle as seen in Table 11. The first two columns in the table show the change in the angle between 4 seconds and 10 seconds. While there is an expected increase in the bending angle in the 100 mW and 200 mW trials, a decrease in the bending angle is seen in the 300 mW, 400 mW, and 500 mW trials. This decrease is due to the shrinking of the sample. When the laser light is incident on the sample, initially, the sample bends due to a temperature gradient caused by the Au NPs in the sample. As the light continues to heat the sample, the temperature gradient equalizes and shrinking sets in. Shrinking was not seen in the 10x samples due to the lowered Au NP concentration. With fewer Au NPs, there are fewer centers of heat generation.

It was also recorded that the 10x samples took about 10 – 30 minutes to relax and return to its original dimensions after the laser was turned off. In contrast, the 20x samples took only 10 – 90 seconds to completely relax once the laser was turned off. This is due to the Au NP concentration present in the samples. With the 20x sample, the Au NP concentration is high enough that there are multiple Au NP end-to-end pathways across the diameter of the sample. Having connected pathways means several avenues of efficient heat dissipation knowing that metals have high thermal conductivity. On the other hand, the 10x samples do not have as many Au NPs and have reduced end-to-end

connections. Thus, 10x samples take longer than 20x samples to relax once a test is complete.

3.2.4 Variable angle tests

With measuring the response of the system to incident light with varying angles, the aim is to have a slope of 1 on the Response angle vs. Incident angle plot. A slope higher than 1 implies the system “over responds” whereas a slope less than 1 indicates the system does not respond adequately. Several arbitrary incident angles were chosen and the response of the system was recorded. All points on the graphs are an average of three data sets. Note that though x axis in the plots for 10x and 20x samples are similar, there are small variations in the incident angle.

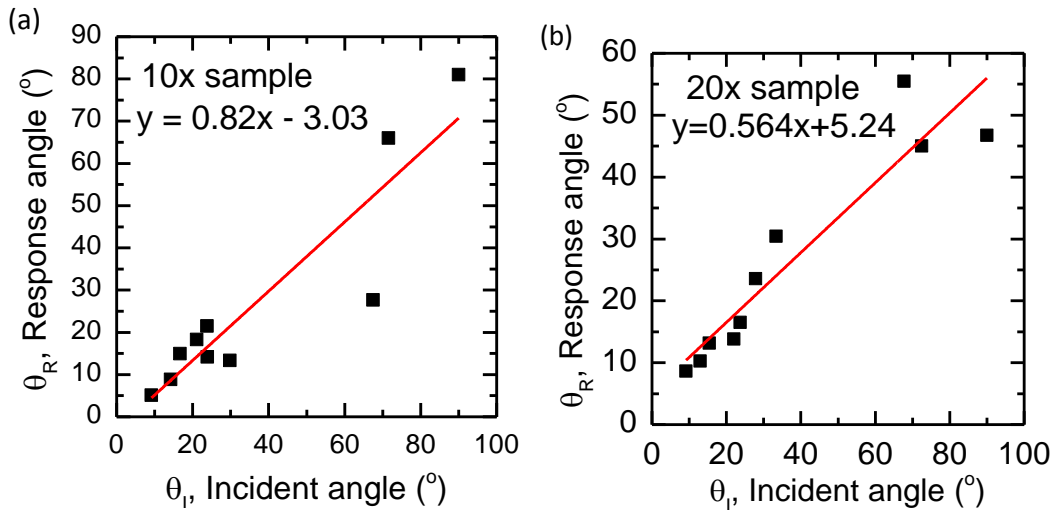


Figure 26: Plots showing the correlation between the incident angle and the response angle from the samples

Table 12: Incident and response angles for the 10x and 20x samples

10x samples		20x samples	
Incident angle ($^{\circ}$)	Response angle ($^{\circ}$)	Incident angle ($^{\circ}$)	Response angle ($^{\circ}$)
16.69	14.97	15.38	13.15
23.83	21.48	23.67	16.53
9.17	5.13	9.16	8.63
14.18	8.86	12.96	10.24

21.07	18.32	21.98	13.82
23.86	14.14	27.83	23.59
29.76	13.32	33.40	30.43
67.46	27.66	67.72	55.50
71.55	66.02	72.48	45.00
90.00	80.98	90.00	46.76

Figure 26 plots the bending angle of the sample in response to the light incident at different arbitrary angles. Slopes of 0.82 for the 10x sample and 0.56 for the 20x sample were calculated. The R^2 value for the 10x sample is 0.84 while the 20x sample has a value of 0.88. The 10x sample bends more accurately to the incident angle. The slopes from the variable angles tests indicate an optimal Au NP concentration which lies between 10x and 20x. This optimal point can be understood as a tradeoff between heat generators and hydrogel in the system. A higher concentration of Au NPs in the system ensures heat generation but does not enhance the accuracy of bending. A lower concentration of Au NP in the system implies less heat being produced. We have designed and characterized a system that is photo-thermo-responsive making it a viable material for a phototropic system.

Chapter 4: CONCLUSIONS AND FUTURE WORK

Attempts at fabricating uniform Au NPs 40 nm in diameter were made. However, particle sizes around 20 nm were achieved. Reducing the trisodium citrate concentration did increase the particle size in an uncontrollable manner. Analysis of the six batches attempted indicated a non-uniform particle size. For a given batch, a conclusive particle size could not be obtained. The swelling ratios for the lower Au NP concentration hydrogel samples were obtained to be 2.9, 3.2, and 2.23 for constrained samples with 0x, 0.1x, and 0.2x Au NP, respectively. Samples for the constrained swelling ratio tests were printed using the P μ SL. For unconstrained tests, the swelling ratios for the 0x, 0.1x, 0.2x, and 0.3x samples were 1.45, 1.64, 1.7 and 1.57, respectively.

Macro-samples with varying compositions were tested with a halogen lamp. Results of tests in different configurations showed that their preferential bending behavior was due to the sample making method and not due to photo-thermal actuation. This was further proved when the same samples did not actuate when illuminated by a green LED lamp. The layer by layer curing fabrication method induced a stiff and soft bilayer effect in the samples. This led to samples bending preferentially towards the soft layer of the sample.

From the focused study tests, we know that the swelling ratios for the 10x and the 20x samples are 1.78 and 1.81, respectively when actuated by heat. Laser actuated tests result in a greater swelling ratio of 2.41 and 3.37 for the 10x and 20x samples, respectively. The difference in the swelling ratios is due to the heating methods. With the laser induced swelling ratio, there is constant and more effective heat generation. Bending angle tests showed varying degrees of response based on the intensity of the incoming laser. In the

20x samples, there was a decrease in the bending angle after about five seconds. This is due to the sample shrinking after it has bent (differential shrinking across the sample). Bending of up to 88° was observed in the 10x samples while 60° was the maximum bending seen in 20x samples. Relaxation times of 30 minutes for the 10x samples and 90 seconds for the 20x samples were observed. Due to the Au NP concentration in the 20x samples, heat dissipation was more efficient.

To show the adaptability of the system in a phototropic setting, variable angle tests were conducted. A slope of 0.82 for the 10x samples and a slope of 0.56 for the 20x samples were calculated. A slope of 1 on the Response angle vs. Incident angle graph would be ideal for a heliotropic system. This implies that the mechanism will always face the direction of incident light at a 90° angle. The ideal system will not over bend or under bend.

With all the experiments conducted, a better understanding of the swelling/shrinking behavior, effect of Au NP concentration on the bending and the response to incident light was obtained.

FUTURE WORK

To complete the characterization of the system, the following experiments can be carried out.

- i) Heating curve swelling ratio experiments: This will give a complete picture of the hysteresis loop. Evidence of hysteresis was seen when cooling curve swelling ratio

data was being recorded. This will give insight into the behavior of the sample as it gets actuated.

- ii) Intermediate Au NP concentrations: Heat and light induced swelling ratio tests, bending angle tests and variable angle tests of samples with intermediate Au NP concentrations. The trend with the Response angle vs. Bending angle shows that the 10x samples have a 0.82 slope. Samples with 7x or 8x Au NP may have a slope closer to 1.
- iii) Heat induced bending: With the help of an IR source, heat induced bending can be explored. This would give insight into the roles and effectiveness of heat and light induced bending when juxtaposed.
- iv) Including other heat generators: Incorporating other heat generators such as graphene oxide, carbon nanotubes and carbon black can help utilize a wider range of the EM spectrum. It may also enhance the efficiency of absorption and photo-thermo energy conversion.

REFERENCES

1. Sherry, R. a. & Galen, C. The mechanism of floral heliotropism in the snow buttercup, *Ranunculus adoneus*. *Plant, Cell Environ.* **21**, 983–993 (1998).
2. Kami, C. *et al.* Nuclear phytochrome A signaling promotes phototropism in *Arabidopsis*. *Plant Cell* **24**, 566–76 (2012).
3. Lubitz, W. D. Effect of manual tilt adjustments on incident irradiance on fixed and tracking solar panels. *Appl. Energy* **88**, 1710–1719 (2011).
4. Alboteanu, L., Manolea, G. & Ravigan, F. Positioning systems for solar panels placed in isolated areas. *Proc. Int. ...* 163–168 (2006). at <http://elth.ucv.ro/fisiere/anale/2006/3_6.pdf>
5. BIAN, Q. Solar photovoltaic roof system based on GPS tracking positioning system. (2011). at <<http://worldwide.espacenet.com/publicationDetails/biblio?DB=EPODOC&II=0&ND=3&adjacent=true&FT=D&date=20110615&CC=CN&NR=201865263U&KC=U>>
6. Li, C., Liu, Y., Huang, X. & Jiang, H. Direct Sun-Driven Artificial Heliotropism for Solar Energy Harvesting Based on a Photo-Thermomechanical Liquid-Crystal Elastomer Nanocomposite. *Adv. Funct. Mater.* **22**, 5166–5174 (2012).
7. Chandler, D. Sun-tracking device wins student prize. *TechTalk* **53**, 6 (2008).
8. Hamilton, T. SunSaluter, developed by 19-year-old Canadian Eden Full, could lower cost of solar PV for world's poorest. *Cleanbreak* (2011). at <<http://www.cleanbreak.ca/2011/06/10/sunsaluter-developed-by-19-year-old-canadian-eden-full-could-lower-cost-of-solar-pv-for-worlds-poorest/>>
9. SunSaluter - Our Solution. at <<http://www.sunsaluter.com/howitworks.html>>
10. Callister, W. & Rethwisch, D. *Materials science and engineering: an introduction. Materials Science and Engineering* **94**, (2007).
11. Burmistrova, A. Temperature-induced swelling / shrinking behavior of adsorbed PNIPAM microgels. (2011).
12. Estroff, L. a. & Hamilton, A. D. Water gelation by small organic molecules. *Chem. Rev.* **104**, 1201–1217 (2004).

13. Ahmed, E. M. Hydrogel: Preparation, characterization, and applications: A review. *J. Adv. Res.* **6**, 105–121 (2015).
14. Peppas, N. a., Huang, Y., Torres-Lugo, M., Ward, J. H. & Zhang, J. Physicochemical foundations and structural design of hydrogels in medicine and biology. *An rnuual Rev. Biomed. Engeniery* **2**, 9–29 (2000).
15. Thipmonta, N. Thermally sensitive conducting hydrogels. 1–259 (2013).
16. Rogovina, L. Z., Vasil'ev, V. G. & Braudo, E. E. Definition of the concept of polymer gel. *Polym. Sci. Ser. C* **50**, 85–92 (2008).
17. Samchenko, Y., Ulberg, Z. & Korotych, O. Multipurpose smart hydrogel systems. *Adv. Colloid Interface Sci.* **168**, 247–262 (2011).
18. Seliktar, D. Designing Cell-Compatible Hydrogels for Biomedical Applications. *Science (80-.).* **336**, 1124–1128 (2012).
19. De Giglio, E. *et al.* PHEMA-based thin hydrogel films for biomedical applications. *J. Bioact. Compat. Polym.* **26**, 420–434 (2011).
20. Schattling, P., Jochum, F. D. & Theato, P. Multi-stimuli responsive polymers – the all-in-one talents. *Polym. Chem.* **5**, 25–36 (2014).
21. Tokarev, I. & Minko, S. Stimuli-responsive hydrogel thin films. *Soft Matter* **5**, 511–524 (2009).
22. Mateescu, A., Wang, Y., Dostalek, J. & Jonas, U. *Thin Hydrogel Films for Optical Biosensor Applications. Membranes* **2**, (2012).
23. Stuart, M. a C. *et al.* Emerging applications of stimuli-responsive polymer materials. *Nat. Mater.* **9**, 101–113 (2010).
24. Young, C. D., Wu, J. R. & Tsou, T. L. Fabrication and characteristics of polyHEMA artificial skin with improved tensile properties. *J. Memb. Sci.* **146**, 83–93 (1998).
25. Yang, C. *et al.* A green fabrication approach of gelatin/CM-chitosan hybrid hydrogel for wound healing. *Carbohydr. Polym.* **82**, 1297–1305 (2010).
26. Ionov, L. Hydrogel-based actuators: possibilities and limitations. *Mater. Today* **17**, 494–503 (2014).
27. Ward, M. a. & Georgiou, T. K. Thermoresponsive polymers for biomedical applications. *Polymers (Basel).* **3**, 1215–1242 (2011).

28. Karg, M. & Hellweg, T. New ‘smart’ poly(NIPAM) microgels and nanoparticle microgel hybrids: Properties and advances in characterisation. *Curr. Opin. Colloid Interface Sci.* **14**, 438–450 (2009).
29. Tsuji, S. & Kawaguchi, H. Colored thin films prepared from hydrogel microspheres. *Langmuir* **21**, 8439–42 (2005).
30. Schild, H. G. Poly (N-Isopropylacrylamide): Experiment , Theory and Application. *Prog. Polym. Sci.* **17**, 163–249 (1992).
31. Zhao, X. *et al.* A kind of smart gold nanoparticle-hydrogel composite with tunable thermo-switchable electrical properties. *New J. Chem.* **30**, 915–920 (2006).
32. Chambon, P. *et al.* Poly(N-isopropylacrylamide) branched polymer nanoparticles. *Polym. Chem.* **2**, 941 (2011).
33. Liu, Y.-J. *et al.* Non-monotonous variation of the LCST of light-responsive, amphiphilic poly(NIPAM) derivatives. *Soft Matter* **8**, 8446 (2012).
34. Murugadoss, A., Khan, A. & Chattopadhyay, A. Stabilizer specific interaction of gold nanoparticles with a thermosensitive polymer hydrogel. *J. Nanoparticle Res.* **12**, 1331–1348 (2010).
35. White-Ziegler, C. a., Malhowski, A. J. & Young, S. Human body temperature (37°C) increases the expression of iron, carbohydrate, and amino acid utilization genes in Escherichia coli K-12. *J. Bacteriol.* **189**, 5429–5440 (2007).
36. Constantin, M. Lower critical solution temperature versus volume phase transition temperature in thermoresponsive drug delivery systems. *Express Polym. Lett.* **5**, 839–848 (2011).
37. Budhlall, B. M., Marquez, M. & Velev, O. D. Microwave, photo- and thermally responsive PNIPAm-gold nanoparticle microgels. *Langmuir* **24**, 11959–66 (2008).
38. Schmidt, S., Motschmann, H., Hellweg, T. & von Klitzing, R. Thermoresponsive surfaces by spin-coating of PNIPAM-co-PAA microgels: A combined AFM and ellipsometry study. *Polymer (Guildf)*. **49**, 749–756 (2008).
39. Wei, J. & Yu, Y. Photodeformable polymer gels and crosslinked liquid-crystalline polymers. *Soft Matter* **8**, 8050 (2012).
40. Xia, L.-W. *et al.* Nano-structured smart hydrogels with rapid response and high elasticity. *Nat. Commun.* **4**, 1–11 (2013).

41. Suzuki, A. & Tanaka, T. Phase transition in polymer gels induced by visible light. *Nature* **346**, 345–347 (1990).
42. Morones, J. R. & Frey, W. Room temperature synthesis of an optically and thermally responsive hybrid PNIPAM–gold nanoparticle. *J. Nanoparticle Res.* **12**, 1401–1414 (2010).
43. Tomatsu, I., Peng, K. & Kros, A. Photoresponsive hydrogels for biomedical applications. *Adv. Drug Deliv. Rev.* **63**, 1257–1266 (2011).
44. Imao, S., Nishi, H. & Kobatake, S. Thermo- and photoresponsive reversible changes in localized surface plasmon resonance of gold nanoparticles covered by poly(N-isopropylacrylamide) with photochromic diarylethene end group. *J. Photochem. Photobiol. A Chem.* **252**, 37–45 (2013).
45. Tsuboi, Y., Nishino, M. & Kitamura, N. Laser-Induced Reversible Volume Phase Transition of a Poly(N-isopropylacrylamide) Gel Explored by Raman Microspectroscopy. *Polym. J.* **40**, 367–374 (2008).
46. Neuburger, N. A. & Eichinger, B. E. Critical Experimental Test of the Flory-Rehner Theory of Swelling. *Macromolecules* **21**, 3060–3070 (1988).
47. Li, M., Bresson, B., Cousin, F., Fretigny, C. & Tran, Y. Submicrometric Films of Surface-Attached Polymer Network with Temperature-Responsive Properties. *Langmuir* **31**, 11516–11524 (2015).
48. Lee, E., Lee, H., Yoo, S. II & Yoon, J. Photothermally triggered fast responding hydrogels incorporating a hydrophobic moiety for light-controlled microvalves. *ACS Appl. Mater. Interfaces* **6**, 16949–55 (2014).
49. Kaneko, T. *et al.* Shape memory gels with multi-stimuli-responses. **3669**, 199–208 (1999).
50. Fan, X., Zheng, W. & Singh, D. J. Light scattering and surface plasmons on small spherical particles. *Light Sci. Appl.* **3**, e179 (2014).
51. Mayer, K. M. & Hafner, J. H. Localized surface plasmon resonance sensors. *Chem. Rev.* **111**, 3828–3857 (2011).
52. Link, S. & El-Sayed, M. a. Size and Temperature Dependence of the Plasmon Absorption of Colloidal Gold Nanoparticles. *J. Phys. Chem. B* **103**, 4212 (1999).
53. Petryayeva, E. & Krull, U. J. Localized surface plasmon resonance: Nanostructures, bioassays and biosensing—A review. *Anal. Chim. Acta* **706**, 8–24 (2011).

54. Turkevich, J., Garton, G. & Stevenson, P. C. The color of colloidal gold. *J. Colloid Sci.* **9**, 26–35 (1954).
55. He, Y. Q., Liu, S. P., Kong, L. & Liu, Z. F. A study on the sizes and concentrations of gold nanoparticles by spectra of absorption, resonance Rayleigh scattering and resonance non-linear scattering. *Spectrochim. Acta Part A Mol. Biomol. Spectrosc.* **61**, 2861–2866 (2005).
56. Peter N. Njoki, I-Im S. Lim, Derrick Mott, Hye-Young Park,† Bilal Khan, Suprav Mishra, Ravishanker Sujakumar, Jin Luo, and C.-J. Z. Size correlation of optical and spectroscopic properties for gold nanoparticles. *J. Phys. Chem. C* **111**, 14664–14669 (2007).
57. Khlebtsov, B. N. & Khlebtsov, N. G. On the Measurement of Gold Nanoparticle Sizes by the Dynamic Light Scattering. *Colloid J.* **73**, 118–127 (2011).
58. Zhu, Z., Senses, E., Akcora, P. & Sukhishvili, S. a. Programmable light-controlled shape changes in layered polymer nanocomposites. *ACS Nano* **6**, 3152–3162 (2012).
59. Sershen, S. R., Westcott, S. L., Halas, N. J. & West, J. L. Independent optically addressable nanoparticle-polymer optomechanical composites. *Appl. Phys. Lett.* **80**, 4609–4611 (2002).
60. Gorelikov, I., Field, L. M. & Kumacheva, E. Hybrid Microgels Photoresponsive in the Near-Infrared Spectral Range Hybrid Microgels Photoresponsive in the Near-Infrared Spectral Range. **126**, 15938–15939 (2004).
61. Shi, S. *et al.* Thermo-, pH-, and Light-Responsive Poly(N-isopropylacrylamide-co-methacrylic acid)-Au Hybrid Microgels Prepared by the in Situ Reduction Method Based on Au-Thiol Chemistry. (2014). doi:10.1021/jp5027477
62. Zhang, E. *et al.* Infrared-driving actuation based on bilayer graphene oxide-poly(N-isopropylacrylamide) nanocomposite hydrogels. *J. Mater. Chem. A* **2**, 15633–15639 (2014).
63. Lee, E., Kim, D., Kim, H. & Yoon, J. Photothermally driven fast responding photo-actuators fabricated with comb-type hydrogels and magnetite nanoparticles. *Sci. Rep.* **5**, 15124 (2015).
64. Jain, P. K., Lee, K. S., El-Sayed, I. H. & El-Sayed, M. A. Calculated absorption and scattering properties of gold nanoparticles of different size, shape, and composition: applications in biological imaging and biomedicine. *J. Phys. Chem. B* **110**, 7238–48 (2006).

65. Abdelhalim, M. A. K. & M. Mady, M. Physical Properties of Different Gold Nanoparticles: Ultraviolet-Visible and Fluorescence Measurements. *J. Nanomed. Nanotechnol.* **03**, 1–5 (2012).